# Synergy and antagonism in the integration of BCR and CD40 signals that control B-cell proliferation

Helen Huang[1,2,3], Haripriya Vaidehi Narayanan[1,2], Alexander Hoffmann[1,2]

[1] Signaling Systems Laboratory, Department of Microbiology, Immunology, and Molecular Genetics (MIMG),
[2] Institute for Quantitative and Computational Biosciences (QCBio),
[3] Bioinformatics Interdepartmental Program,
University of California Los Angeles, Los Angeles, USA.

## ABSTRACT

In response to infection or vaccination, a successful antibody response must enrich high-affinity antigen-reactive B-cells through positive selection, but eliminate auto-reactive B-cells through negative selection. B-cells receive signals from the B-cell receptor (BCR) which binds the antigen, and the CD40 receptor which is stimulated by neighboring T-cells that also recognize the antigen. How BCR and CD40 signaling are integrated quantitatively to jointly determine B-cell fate decision and proliferation remains unclear. To investigate this, we developed a differential-equations-based model of the BCR and CD40 signaling networks activating NFκB. Our model accurately recapitulates the NFκB dynamics of B-cells stimulated through their BCR and CD40 receptors, correctly predicting that costimulation induces more NFκB activity. However, when linking it to established cell fate decision models of cell survival and cell cycle control, it predicted potentiated population expansion that was not observed experimentally. We found that this discrepancy was due to a time-dependent functional antagonism exacerbated by BCR-induced caspase activity that can trigger apoptosis in founder cells, unless NFκB-induced survival gene expression protects B-cells in time. Guided by model predictions, sequential co-stimulation experiments revealed how the temporal dynamics of BCR and CD40 signaling control the fate decision between negative and positive selection of B-cell clonal expansion. Our quantitative findings highlight a complex non-monotonic integration of BCR and CD40 signals that is controlled by a balance between NFκB and cell-death pathways, and suggest a mechanism for regulating the stringency of B-cell selection during an antibody response.

## Keywords

Germinal center reaction, B-cell selection, CD40 signaling, BCR signaling, NFκB, activation-induced cell death, mathematical modeling, systems immunology

## Highlights

- CD40 and BCR signaling in B-cells synergize to potentiate NFκB cRel activation
- BCR-apoptotic signaling may enhance or antagonize CD40-driven proliferation
- BCR-induced apoptosis may be rescued by CD40 within a temporal window
- A mathematical model reveals regulators of the dose-dependent selection stringency

## INTRODUCTION

A critical component of the immune response is the generation of antibody. In order to generate antigen-reactive antibodies, B-cells evolve in the germinal center (GC), where they mutate their B-cell receptor (BCR) sequences, and are subjected to selection based on their interactions with antigens and helper T-cells (Nowosad, Spillane and Tolar, 2016). Based on clonal selection theory, high-affinity antigen-reactive B cells receive a stronger stimulus and hence proliferate to a greater extent, while low-affinity B cells receive a weaker stimulus and do not proliferate as much (Burnet, 1957; Victora and Nussenzweig, 2022). But a successful response must not only enrich high-affinity antigen-reactive B-cells through positive selection, but must also eliminate autoreactive B-cells by negative selection. Thus, the stimuli acting on GC B-cells determine the outcome between positive and negative selection.

B-cells receive two stimuli: they are stimulated briefly through their BCRs while picking up antigens from neighboring follicular dendritic cells (FDCs), followed by a period when they search for a T follicular helper cell (Tfh) that will stimulate them through their CD40 receptor. The BCR is a dual-purpose receptor, functioning both to endocytose antigen and present it to T-cells and to initiate signaling. However, how the signaling functions of the BCR are relevant to the selection of B-cells in the GC remains unclear. Prior studies demonstrated that BCR signal transduction was short-circuited in GC B-cells (Khalil, Cambier and Shlomchik, 2012) and that the CD40 signal alone may be sufficient for B-cell clonal expansion (Shulman *et al.*, 2014), while others suggested that BCR signaling is necessary for the survival and priming of GC B-cells for their positive selection (Chen *et al.*, 2023). Overall, although both BCR and CD40 signaling have been profiled experimentally (Damdinsuren *et al.*, 2010; Akkaya *et al.*, 2018), there is a lack of quantitative understanding of how these two signaling events are integrated within the dynamic sequence of those interactions. A mathematical model is thus needed to understand how the two signals interact and jointly determine the appropriate B-cell survival and proliferation to maintain a balance in positive and negative selection.

Both BCR and CD40 signaling pathways converge on the nuclear factor kappa B (NFκB) signaling system. While BCR stimulation activates the canonical NFκB pathway only transiently, CD40 stimulates both the canonical and noncanonical pathways, resulting in prolonged NFκB activity (Sen, 2006). Mathematical models of the NFκB signaling system have been established (Mitchell *et al.*, 2023) and they have been integrated with models of cell fate decision circuits to

recapitulate *in vitro* B-cell population dynamics resulting from the toll-like receptor ligand CpG, a T-independent stimulus (Shokhirev *et al.*, 2015; Mitchell *et al.*, 2018; Roy *et al.*, 2019). Another set of models explored the feedback mechanisms within the BCR molecular network, which involves protein kinase C β (PKCβ), CARD containing MAGUK protein1 (CARMA1), transforming growth factor β-activated kinase 1 (TAK1) and IκB kinase β (IKKβ) (Shinohara *et al.*, 2014, 2016; Inoue *et al.*, 2016). However, despite many studies of the CD40 signaling pathway (Dadgostar *et al.*, 2002; Elgueta *et al.*, 2009; Akiyama, Shinzawa and Akiyama, 2012), there is no mathematical model or quantitative understanding of the dynamics of CD40 signaling. Further, no work has been done to combine the BCR and CD40 receptor signaling knowledge and explore how the two signals combine quantitatively to control NFκB signaling and resulting cell fate decisions such that the B-cell population dynamics in response to T-dependent stimulation may be understood or predicted.

Here, we undertook quantitative studies to develop mathematical models for the receptor activation modules of the BCR and CD40. We then tested the reliability of these models by linking them to established cell survival and cell cycle models for quantitative studies of the B-cell population dynamics in response to BCR and CD40 receptor stimulation. The combined model correctly recapitulated the population dynamics data of B-cells stimulated with either stimulus, but simulating the combined stimulus conditions revealed discrepancies with experimental data. Our investigations revealed an unexpected time-dependent functional antagonism that modules the expected synergy between BCR and CD40 signaling. It is exacerbated by BCR-induced caspase activity that can trigger apoptosis in founder cells, unless NFκB-induced survival gene expression protects B-cells in time. Model-guided sequential co-stimulation studies then revealed how temporal signaling dynamics regulate the control of cell fate decisions that underlie negative vs. positive selection of B-cell clonal expansion.

## RESULTS

### A mathematical model of B-cell signaling during T-dependent stimulus responses

To understand how BCR and CD40 signaling are mechanistically integrated during T-dependent (TD) immune responses, we developed a mathematical model of the molecular interaction network that downstream of these receptors. We built on an established mathematical model of the BCR signaling pathway (Inoue *et al.*, 2016) and formulated a new CD40 model to include key mechanistic features of its known signaling pathway (Elgueta *et al.*, 2009; Akiyama, Shinzawa and Akiyama, 2012). Both BCR and CD40 pathways culminate in canonical and non-canonical IKK activation, defining a T-dependent B-cell signaling network model that includes 37 mass-action equations (Fig. 1A). We parameterized the T-dependent B-cell signaling network model by adopting parameter values from established models, using half-lives and synthesis rates from biochemical experiments in the literature, or manually fitting to published time course data (Table 1: parameter values).

Stimulation of B cells with TD ligands activates the multi-dimeric NFκB signaling system to regulate downstream cell fate response. Therefore, once the receptor model outputs appeared

to fit the published activation dynamics of IKK induced by TD stimuli (Shinohara *et al.*, 2016), we connected it to the latest mathematical model of the NFκB signaling network that accounts for the time-dependent activity of multiple NFκB dimers (Mitchell *et al.*, 2023) (Fig. 1B). We then introduced heterogeneity to the signaling dynamics by sampling parameter sets from parameter distributions (see more details in "Computational modeling of the T-dependent receptor signaling pathway" section of the Methods). To test if the BCR/CD40-NFκB model recapitulates the NFκB dynamics induced by TD stimulation, we stimulated naïve B cells for 7, 24, and 48 hours with different stimulation conditions – low α-CD40 concentration (1μg/mL), high α-CD40 concentration (10μg/mL), and costimulation with high concentration of both α-CD40 and α-BCR (10μg/mL) – to quantify their NFκB signaling activity by immunoblotting the nuclear fraction for RelA (p65) and cRel level (Fig. S1A), following live cell normalization (Fig. S1B).

The optimal range of experimental doses of α-CD40 were chosen based on prior literature that carefully examined the B cell proliferation response to defined α-CD40 concentrations (Rush and Hodgkin, 2001; Turner, Hawkins and Hodgkin, 2008; Hawkins *et al.*, 2013). The chosen experimental doses were determined to be equivalent to model simulations with 6nM of stimulus for low dose and 30nM for high dose. We then undertook a systematic dose-response analysis focusing on NFκB, and found that peak nuclear RelA:p50 (Fig. 1C) and nuclear cRel:p50 (Fig. 1D) reach saturation with the high dose, but that cRel:p52 does not. This indicates that the canonical and non-canonical NFκB activities have differential dose responses in response to CD40 stimulation. Thereby the low dose of α-CD40 allows us to examine how BCR and CD40 signals are integrated in unsaturated NFκB conditions; while the high dose of α-CD40 allows us to test their integration under saturated canonical NFκB condition.

The integrated model recapitulated the amplitude, dose-responsiveness, and speed of RelA and cRel dynamics in response to various stimulation schemes (Fig. 1E-H). For example, in both simulated and experimental data, nuclear RelA level in B-cells stimulated with high and low doses of α-CD40 increased 10- and 5-fold, respectively, after 7 hours of stimulation (Fig. 1E-F), and nuclear cRel was induced to around 13- and 4-fold relative to its steady-state level (Fig. 1G-H). The model further captured the steeper gradient of downregulation of nuclear cRel than RelA from 7hrs to 24hrs after stimulation. Although both model simulation and immunoblot results showed a decrease in nuclear NFκB levels at 24hrs after stimulation, *in vitro* data indicated a slight rebound at 48hrs (Fig. 1F,H), whereas the *in silico* levels continued to decrease (Fig. 1E,G). This discrepancy in late-phase NFκB dynamics could be due to *in vitro* cells undergoing cell death or proliferation by this timepoint (Fig. S1B), which this signaling-only model does not account for. In sum, the model was able to recapitulate early B-cell NFκB dynamics in response to TD stimulation, but failed to capture late activity in the absence of accounting for cell fate decisions.

**Combining models of signaling and cell fate decisions**

Given that NFκB dynamics are critical determinants of B-cell fate decisions (Shokhirev *et al.*, 2015; Mitchell *et al.*, 2018; Roy *et al.*, 2019), we next asked whether linking the CD40-NFκB signaling model to cell fate decision models would correctly predict the population dynamics in response to TD stimulation. After connecting these modules (Fig. 2A left), we could simulate the

time-dependent dynamics of successive generations of B-cells that results from division and death decisions. To generate experimental data for comparison, we stained naïve B cells with the Cell Trace Far Red (CTFR) dye, cultured them under various anti-CD40 stimulus conditions to observe their proliferation kinetics *via* dye dilution (Fig. S1C), and quantified the number of cells under each generation using FlowJo's generation deconvolution feature (Roederer, 2011) (Fig. 2A right). Four conditions were used in the experiment and model simulation, respectively: no stimulus, low concentration (1μg/mL in experiment, which corresponds to 6nM in model simulation), medium concentration (3μg/mL / 20nM), and high concentration (10μg/mL / 60nM) of α-CD40 stimulus.

Inspecting the data, we found that increasing doses of CD40 affect both the time to first division (Tdiv0) and the total number of divisions a B-cell can reach, while T-independent (TI) ligands CpG and LPS, which were used prior studies, show fast Tdiv0 even at low doses (Hawkins *et al.*, 2013). Our published cell fate module that was tuned to B-cells stimulated with the TI ligand CpG (Shokhirev *et al.*, 2015; Mitchell *et al.*, 2018; Roy *et al.*, 2019) qualitatively fit the TD ligand CD40 data, but the simulated responses were faster than observed (Fig. S2A). Meanwhile, the later division times (Tdiv1+) of the CD40 experimental data were shorter than predicted by the model (Fig. S2A), while the proportion of dividers was lower. To improve the model fit, we identified locally sensitive parameters in the cell cycle module that contribute to Tdiv0 and Tdiv1+ by calculating the standard deviation in division times when scaling each parameter from 0.2 to 5.0 times the original values (Fig. S2C, see more details in "Local sensitivity analysis to tune CD40-activated cell fates" section of the Methods). After fine-tuning the sensitive parameters, the model appeared to recapitulate key aspects of B-cell population dynamics in response to all tested CD40 doses (Fig. 2B-C). For example, the fold change of live cell counts and the proportion of generation 0 cells (non-dividers) relative to generation 1+ cells (dividers) appeared to be consistent between model simulation and experimental results at most time points; both features were also captured by the model in a dose-dependent manner.

To quantitatively evaluate the model fit at the population dynamics level, we calculated the root mean square deviation (RMSD) of the population expansion index (Fig. 2D) and generational composition (Fig. 2E) between model and experimental outputs at each experimental timepoint (0, 24, 36, 48, 72, and 96 hrs). Total RMSDs were evaluated between each model and experiment pair, regardless of matching and mismatching CD40 doses. As a permutation null, the dose-mismatched pairs demonstrated high RMSD values of around or above 1.0, while the dose-matched pairs exhibited much lower RMSD values of around or below 0.5 for population expansion index, indicating great fit in all CD40 doses (Fig. 2D, right). This marked an improvement from the RMSD values before tuning the cell fate parameters. For example, before tuning, population expansion of B-cells stimulated with a medium dose *in silico* had a 1.00 RMSD from its matched *in vitro* medium dose, higher than its 0.75 RMSD from the mismatched high dose (Fig. S2B, top). After tuning, medium dose *in silico* data had a 0.45 RMSD from the matched *in vitro* medium dose data, much lower than its 1.33 RMSD from the mismatched high dose (Fig. 2D, right). In sum, the multi-scale model was able to reliably predict B-cell population dynamics over 96hrs in terms of heterogeneous receptor-induced NFκB signaling dynamics and ensuing cell death and division decisions.

**BCR and CD40 costimulation show both synergy and antagonism**

As the model captured B-cell population dynamics in response to various doses of CD40 stimulation, we next asked if it can accurately predict the dynamics in response to BCR and CD40 costimulation. We followed the same workflow as in Fig. 2A to generate model simulation and dye dilution data in response to two BCR and CD40 costimulation conditions: first, high α-IgM (10μg/mL) and low α-CD40 (1μg/mL) (co-low) and second, high α-IgM (10μg/mL) and high α-CD40 (10μg/mL) (co-high). In both cases, the multi-scale model predicted more population expansion in costimulation (Fig. 3A and 3C) than the corresponding high and low CD40 single-ligand stimulation (Fig. 2B). Because both BCR and CD40 stimuli activate the pro-survival and pro-proliferative NFκB pathway, the model simulation results were consistent with our expectation of synergistic population expansion.

However, experimental results of matching stimulus conditions revealed that the two TD stimuli synergized only in a dose-dependent manner. While the dye dilution data (Fig. 3B) showed a synergistic population expansion in co-low condition as predicted (Fig. 3A), there was an unexpected antagonistic effect of α-IgM costimulation when combined with high CD40 stimulation (Fig. 3D). Indeed, when we calculated the RMSDs between simulated and experimental data for the 2 costimulation conditions, the co-low condition had a score of 0.93, indicating a good fit that's comparable to the CD40 single-ligand stimulation conditions (that ranged from 0.32 to 0.90), but the co-high condition had a bigger deviation of 1.58, suggesting a poorer fit (Fig. 3E). Notably, the poor RMSD in co-high condition was mainly attributed to the population expansion index, which had an RMSD of 0.89 that's much higher than its 0.25-to-0.45 range in CD40 single stimulation conditions (Fig. 2D, right), while the generation composition RMSD was 0.68, only slightly above its 0.06 to 0.53 range in CD40 single stimulation conditions (Fig. 2E, right).

To better understand the source of discrepancy between simulated and experimental population dynamics, we next examined the experimental effects of high α-IgM on the background of CD40 stimulation. High α-IgM costimulation seemed to have a positive effect on B-cells stimulated with a low concentration of CD40, increasing both the population expansion index (Fig. 3F) and proliferative capacity (Fig. 3G). The RMSD scores between these two experimental conditions also highlighted that high α-IgM costimulation deviated in both population expansion and generation composition (Fig. 3H). In the context of high CD40 stimulation, however, the addition of high α-IgM had a less straightforward effect, causing the B-cell population to expand less at 96 hours than without α-IgM (Fig. 3I). Conversely, the generation composition chart showed a similar proliferation profile in both conditions, and even slightly earlier Tdiv0 values in costimulation (Fig. 3J). Consistent with figures 3I-J, the RMSD between these two experimental conditions suggested that the addition of high α-IgM to high CD40 predominantly altered B-cell population expansion, without significantly changing its proliferative capacity (Fig. 3K). High α-IgM thus inflicted opposite effects on B-cell population dynamics, depending on a background of low or high dose of CD40. In sum, the model appeared to accurately predict the NFκB-dependent synergistic signaling interaction between BCR and CD40 at low dose of CD40, but failed to reproduce an NFκB-independent antagonistic interaction at co-high dose.

**Considering BCR-induced apoptosis and NFκB saturation**

Since the model did not accurately predict the population dynamics in response to BCR-CD40 costimulation, we searched for a mechanistic explanation. Population expansion is a result of both cell proliferation and cell survival, and BCR stimulation (through α-IgM or *in vivo* antigen) can have pro-proliferative effects on B-cells (Shokhirev and Hoffmann, 2013; Chen *et al.*, 2023). Therefore, the reduced population expansion in the high co-stimulation condition seemed to suggest that α-IgM stimulation had an NFκB-independent anti-survival effect that overrides its pro-survival effect through NFκB signaling. Indeed, it was reported that ligation of the BCR induces cell death in some B cells (Chen *et al.*, 1999; Graves, Craxton and Clark, 2004) due to activation of Bcl-2 Interacting Mediator of cell death (Bim) (Gao, Kazama and Yonehara, 2012), caspase-2 or -8 (Chen *et al.*, 1999), mitochondrial dysfunction (Akkaya *et al.*, 2018), or other pathways. Based on the signaling mechanisms that may mediate activation-induced cell death (AICD) and the available species in the existing cell death module, we revised the T-dependent multi-scale B-cell model to include a simplified pathway from activated BCR to caspase-8 processing (Fig. 4A, see more details in "Computational modeling of BCR-induced cell death" section of the Methods). This processing of pre-caspase-8 into caspase-8 then triggers B-cell death by initiating the cleavage of downstream effector caspases in the cell death module.

To test if the revised model could capture the population dynamics in costimulatory conditions, we re-simulated the virtual B-cell population. With the addition of BCR-induced caspase processing, the simulated cell population in response to co-high stimulation exhibited more cell death and resulted in an overall reduction in population expansion (Fig. 4B, left), which is more consistent with the experimental data (Fig. 4B, right). Meanwhile, Fig. 4C shows slightly less synergy in co-low than previously predicted (Fig. 4A), resulting in more concordance with experimental data as well. A decreased RMSD further confirmed the improvement in model fit (Fig. 4D). Overall, this indicates that the functional antagonism may be mediated by BCR-induced caspase activity triggering apoptosis in founder cells.

To further test the model in which BCR stimulation is pro-proliferative due to NFκB signaling and pro-apoptotic due to AICD, we then asked why the two TD stimuli manifested synergy at co-low stimulation but exhibited antagonism at co-high stimulation. We examined nuclear RelA and cRel dynamics, this time with the involvement of cell fate states, and noticed a much stronger early NFκB signaling synergy in the co-low condition (Fig. 4F) than the co-high stimulation (Fig. 4E). In the context of high CD40 stimulation, the additional high α-IgM costimulation had minimal effects on nuclear RelA and cRel levels in the first 24 hours (Fig. 4E). This lack of early synergy suggested NFκB signaling saturation in high α-CD40 stimulation, such that BCR signal cannot contribute more. On the other hand, in B-cells stimulated with the low, sub-saturating CD40 dose, α-IgM could amplify nuclear RelA and cRel levels (Fig. 4F). In sum, the combination of AICD and NFκB signaling saturation explained the dose-dependent interaction in BCR-CD40 costimulation. These results also demonstrated the model's capacity to capture both early and late B-cell NFκB dynamics in response to TD stimuli when simulations account for cell death and proliferation decisions.

**BCR-induced apoptosis can override BCR-induced population growth**

As the BCR has the potential to activate both pro-survival signaling via NFκB and anti-survival via caspase-8, we next examined the response relationships of these two pathways and whether the net outcome may be dose-dependent. We first validated that the simulated population dynamics fit the experimental data for costimulation with high dose CD40 combined with three doses of BCR (Fig. 5A). We found consistent population dynamics in experimental and simulation studies, in which the dose of BCR stimulus had only subtle effects. We observed that in both model-simulated and experimental populations, the number of non-proliferating cells (lightest gray) is the lowest at 96hrs when costimulated with high BCR, while the proliferating cell populations (darker grays) remain comparable across conditions (Fig. 5B). This indicates that when costimulated with a high CD40 dose, cell survival and overall population expansion monotonically decrease with increasing BCR dose from zero, low, to high.

We next focused on how these stimuli potentially affect cell survival which could censor the proliferation module in the multi-scale model. Simulating B-cells stimulated with various doses of either BCR or CD40, we observed distinct dose-response patterns. For CD40, the higher the dose, the shallower the Kaplan-Meier survival curve is, indicating a monotonic pro-survival effect of CD40 stimulation (Fig. 5C). On the other hand, the survival dose response to BCR stimulation appeared non-monotonic (Fig. 5D), with low-BCR-stimulation increasing the probability of survival over unstimulated cells, but high-BCR-stimulation actually reducing the probability of survival. When we quantified the number of surviving cells in the first 24hrs (Fig. 5E), we clearly observed the difference between the two distinct dose-response patterns in terms of monotonicity for CD40 vs BCR agonists.

To gain a systematic understanding of the effects of BCR-induced apoptosis on B-cell response in all combinations of BCR and CD40 doses, we simulated 25 single or costimulation scenarios, each with 1000 founder B-cells. We then used locally estimated scatterplot smoothing (LOESS) to fit a smooth curve through this scatterplot of 25 data points to generate heatmaps of cell survival rate, proliferation capacity, and population fold-change. Without AICD, we observed monotonic increase in all metrics with respect to both BCR and CD40 doses (Figure 5F-H). When we incorporated AICD in the model, all the metrics still monotonically increased with respect to increasing CD40 doses (5I-K), and the divided cells percentages remained unchanged (5G, J) with little difference in the percentage dividers (5M), as expected. However, with increasing BCR doses at a low (or zero) CD40 dose, the cell survival rate first increases then decreases (5I, left 2 columns). When the CD40 dose is medium or high, increasing doses of BCR monotonically decreased the cell survival rate (5I, right 3 columns). Examining the resulting population fold-change (5H,K), we observed that BCR-induced apoptosis prevented BCR stimulation from promoting population growth, and rendered the B-cell response independent of BCR signaling.

**A limited temporal window of opportunity to acquire CD40 signals**

In TD activation, a B-cell first experiences a BCR signal when binding the antigen, and then a CD40 signal when it has found a T-cell that also recognizes the antigen (Bretscher and Cohn, 1970; Parker, 1993). The time delay between the two signals is determined by the B-cell

searching for T-cell help (Okada *et al.*, 2005). Given that our multi-scale model captured B-cell NFκB and population dynamics in response to all tested doses of CD40 stimulation as well as BCR-CD40 costimulation doses, we asked if it could provide some insights on how the two signals combine in the more physiological TD stimulation scenario of sequential BCR and CD40 stimulation. To simulate this scenario, a one-hour BCR signal was initiated at 0hr, and the CD40 signal was initiated at 1, 3, 5, or 8hrs. In this stimulation scenario using high BCR + low CD40, the multi-scale model predicted that the B-cell population decreases over time, with a steeper decrease when the gap is longer (Fig. 6B, left). In contrast, in the low BCR + high CD40 sequential stimulation condition, the B-cell population increased drastically after 48hrs despite an initial decrease in the first 24 hrs. That initial decrease was faster when the time gap was 8hr than 1hr gap but the resulting population size at 96hrs was similar (Fig. 6B, right). However, when we simulated the high BCR + high CD40 stimulation scenario, the model simulations exhibited a larger variation in population size at 96hrs, where an 8hr gap resulted in less than half the number of live cells than a 1hr or 3hr gap (Fig. 6B, middle). This indicated that there is a limited temporal window of opportunity for B-cells to acquire CD40 signal that rescues a crashing cell population following BCR stimulation.

To test these model predictions, we undertook experiments with these stimulation scenarios. We stained naïve B cells with the Cell Trace Far Red (CTFR) dye, stimulated them with low (1μg/mL) or high (10μg/mL) dose of anti-BCR stimulus for 1hr, washed, and cultured them under low (1μg/mL) or high (10μg/mL) anti-CD40 stimulus conditions at 1, 3, 5, or 8hrs after BCR pre-activation for 4 days (Fig. 6A). We then observed and analyzed their proliferation kinetics *via* dye dilution using the same workflow as in Fig. 2A. Experimental results demonstrated distinct effects of time-gaps on B-cell population dynamics across sequential stimulation conditions (Fig. 6C). Specifically, increasing the time gaps between BCR and CD40 stimulation had relatively small effects on B-cell population fold-change in both high BCR + low CD40 (Fig. 6C, left) and low BCR + high CD40 sequential stimulation (Fig. 6C, right), as the colored lines representing different time-gaps followed each other closely. On the other hand, larger time-gaps (5-8hrs) significantly diminished B-cell population compared to smaller time-gaps (1-3hrs) in high BCR + high CD40 sequential stimulation (Fig. 6C, middle). Surprisingly, the time-gap also appeared to have a non-monotonic effect on B-cell population expansion, where cells stimulated 3hr apart (orange) resulted in higher fold-change than cells stimulated 1hr-apart (red), both *in silico* (Fig. 6B) and *in vitro* (Fig. 6C, middle & right). This may be due to reduced NFκB signaling saturation when the two stimuli were further apart, while being still close enough to allow for rescue from AICD. In sum, the experimental results were consistent with the model simulation, confirming the existence of a limited window of opportunity at the high BCR + high CD40 sequential stimulation regime (Fig. 6C, middle).

Overall, our *in silico* and experimental investigations of the temporal relationship between these antagonistic signals revealed a limited time window within which CD40 signaling may effectively rescue cell death triggered by BCR signaling. The size of the temporal window depends on the strength of the BCR and CD40 signals, but when the time gap exceeds a threshold of about 5 hours, the opportunity to trigger B-cell population expansion is severely diminished.

**Noisy BCR-induced Bcl-xL expression determines the window of opportunity**

We next asked what may determine the window of opportunity and the heterogeneous survival outcomes in single B-cells that are a prerequisite for subsequent population expansion. As BCR stimulation was shown to be both pro-survival due to NFκB-induced Bcl-xL activity and anti-survival due to AICD (Fig. 7A) resulting in a non-linear dose response (Fig. 5), we examined how this paradoxical signaling affects single B-cell responses *in silico* model simulations. In the apoptosis pathway, activation of caspase-8 leads to downstream activation and oligomerization of Bax to the mitochondrial outer membrane, forming Bax pores that trigger mitochondrial outer membrane permeabilization (MOMP). The prominent anti-apoptotic Bcl-xL protects cells from MOMP by sequestrating Bax from oligomerization or by retrotranslocating Bax to the cytosol (Dou *et al.*, 2021).

We first examined Bcl-xL and caspase-8 trajectories in 3 stimulation conditions (Fig. 7B). Noticeably, a decline in free Bcl-xL level (thin lines) correlated with a substantial increase in caspase-8 activity (denoted by a quick color transition from deep blue to pink), the timing of both corresponds to a decline in cell survival (thick line). While CD40 stimulation induces Bcl-xL in a homogeneous manner (Fig. 7B, left), BCR stimulation introduces more heterogeneity in Bcl-xL level among different cells (Fig. 7B, middle and right). Because Bcl-xL is induced by NFκB transcription factors, we also reported RelA and cRel nuclear activity and found that B-cells with higher NFκB activity induced their Bcl-xL levels faster and to a higher extent (Fig. 7C), protecting the cells until the onset of CD40 stimulation. On the other hand, cells with lower NFκB activity could not generate enough anti-apoptotic Bcl-xL and ceased to live (indicated by discontinued lines). Cells that survived the first 12 hours had significantly higher peak RelA, cRel, and Bcl-xL activity than cells that died (Fig. 7D). The variability in BCR-induced nuclear NFκB level was consistent with a previous report (Shinohara et al. 2014), where the TAK1-IKK2 positive feedback resulted in a switch-like behavior in BCR activation.

To gain a systematic understanding of the effects of the time gap between CD40 and BCR stimulation on B-cell response in all combinations of BCR and CD40 doses, we again simulated 25 single or sequential scenarios, each with 1000 founder B-cells, to generate maps of cell survival rate, proliferation capacity, and population fold-change. With a 1hr pulse in BCR stimulation, we observed a cell survival trend (Fig. 7E) similar to that with coincident costimulation than the scenarios in Fig. 5J. With an 8hr staggered stimulation (Fig. 7F), the effect of AICD on cell survival was much stronger than in coincident costimulation (Fig. 5J), showing heightened cell death within the first 24hrs at medium and high BCR doses. The two population size maps in Fig. 7H-I showed very little difference at low CD40 doses but demonstrated the biggest differences in the upper and lower right corners, where virtual B-cells were stimulated with high CD40 doses and either high or no BCR doses (Fig. 7J). Overall, these results clearly illustrated the importance of not only BCR and CD40 stimulation doses but their temporal relationships in determining cell fates and ultimately population expansion.

## DISCUSSION

In this work, we investigated how the BCR-mediated signal I and the CD40-mediated signal II are integrated in the B-cell fate decision process to clarify their roles in T-dependent B-cell selection. Prior work demonstrated that BCR and CD40 signaling synergize at the level of NFκB activation (Damdinsuren *et al.*, 2010), but did not determine how these signals combine to determine the subsequent B-cell fate decisions and thus the emergent population dynamics. Here, we presented a mechanistic mathematical model of B-cell signaling and fate decision in response to T-dependent stimulation scenarios that recapitulates experimental observations (Fig. 1-4) and could be used to explore the biological consequences of the dose and temporal relationship between type I and II signals (Fig. 5-7). We showed that while BCR signaling has the potential to prime B-cells for positive selection by synergizing with CD40 on NFκB signaling (Fig. 3A-B, F-H), it could also initiate negative selection by functionally antagonizing CD40 signaling through AICD (Fig. 3-4). Our work suggests that BCR signaling is the key to tuning the balance between positive and negative selection in mature B-cells.

To construct a tractable mathematical model, we took a parsimonious approach to abstract the signaling pathway initiated by the T-dependent stimuli leading to NFκB. For example, CD40 ligand engagement recruits adapter proteins, which include several tumor necrosis factor receptor-associated factor (TRAF)s, such as TRAF1, TRAF2, TRAF3, TRAF5, TRAF6, and a combination of their complexes (Elgueta *et al.*, 2009). To avoid the complexity of combinatorial biochemical reactions among the TRAF complexes, we used TRAF3 to represent the TRAF2-TRAF3 complex that constitutively inhibits the noncanonical NFκB pathway, and TRAF6 to represent the TRAF1-TRAF2, TRAF3-TRAF5, and TRAF6-TRAF2 complexes that all activate the canonical NFκB pathway. The construction of the CD40 signaling model further included parameters extracted from a substantial literature of experimental studies. For example, the degradation rate of NIK was calculated from its half-life (3hrs) estimated in a pulse-chase assay for B-cells stimulated with BAFF and anti-CD40 (Qing, Qu and Xiao, 2005). The differential degradation rates of CD40 receptor (CD40R) and ligated CD40R (CD40LR) were obtained from cell surface biotinylation assay at the surface of 9HTEo- epithelial cells (Tucker and Schwiebert, 2008); similar parametrization applied to the internalization rates of BCR and antigen-ligated BCR (ABCR) (Coulter *et al.*, 2018). Furthermore, the rates of association and dissociation between CD40 and anti-CD40 were derived from the Ka and Kd values determined by surface plasmon resonance (SPR) binding analysis (Ceglia *et al.*, 2021). Having incorporated substantial molecular details and biochemical data, the model serves as a framework for an *in-silico* laboratory that could be expanded and revised iteratively with wet-lab experiments for mechanistically investigating the effects of various genetic and pharmacological perturbations on T-dependent-activated B-cell NFκB dynamics.

Our previous work identified NFκB as a key determinant of B-cell population dynamics, and quantified the relative contributions of cRel- and RelA-containing NFκB dimers to downstream cell fate effector functions (Shokhirev *et al.*, 2015; Roy *et al.*, 2019). Here, we present an extended mathematical model, which demonstrated that NFκB-induced survival and proliferation as well as BCR-activation-induced apoptosis are sufficient to explain the survival and proliferation kinetics of B-cells in the explored conditions. Although other signaling pathways that are induced by BCR and CD40, such as PI3K and MAPK, could also play a role, without

perturbation studies of these pathways their roles are not quantifiable and are only implicit in the current mathematical model. Previous work concluded that the NFκB signaling pathway, but not PI3K, dominates the primary response to CD40 stimulation in GC B-cells (Luo, Weisel and Shlomchik, 2018). In response to TD stimuli, the roles of the MAPK p38 and ERK pathways are thought to be minor and generally cooperative with NFκB (Dadgostar *et al.*, 2002). We used naive B-cells isolated from the spleen for experimental studies that allowed us to obtain granular datasets on signaling dynamics and cell fate decisions with the dynamic population response. The possibility that B-cells may behave differently in the *in vivo* lymph node GC microenvironment (Young and Brink, 2021) could affect the reliability of extrapolating our conclusions from the present study to the *in vivo* phenomena of positive and negative selection. Still, Silva et al. showed that treatment with antigen bearing only the immunodominant epitope during the early GC response selectively suppressed those GC B-cells, and in turn promoted subdominant GC B-cells in mice immunized with both antigens (Silva *et al.*, 2017). This confirmed the ability of BCR signaling to modulate positive and negative selection in GC B-cells, and is consistent with our observations of BCR-CD40 antagonism.

To fit the temporal dynamics of the model-simulated proliferative response to TD stimulation, we tuned a few parameters in the cell cycle model that was adopted from our previous work on TI ligand CpG (Fig. S2). CD40 generally stimulates a stronger NFκB activity than CpG at saturating doses as CD40 activates also the non-canonical pathway, thereby relieving the IκBδ brake on canonical signaling (Rodriguez *et al.*, 2024). However, the proliferative response to CpG is faster and stronger, suggesting that another pathway, such as MAPK which is strongly induced by the MyD88 adaptor (Caldwell *et al.*, 2014; Cheng *et al.*, 2017), may be responsible for boosting cell cycle entry in response to some TI stimuli. Our revised model based on the CD40 stimulus that does not activate much MAP p38 pathway is thus more accurate in recapitulating the control of cell growth and cell cycle in response to NFκB.

Our work revealed a non-monotonic integration of BCR and CD40R signals in the proliferative responses of B-cells, due to BCR-induced apoptosis and NFκB signaling saturation (Fig. 4). Consistent with previous research which suggested that CD40 signaling alone was sufficient for B-cell affinity maturation (Victora *et al.*, 2010; Shulman *et al.*, 2014), we found that BCR-induced apoptosis prevented BCR stimulation from promoting additional population growth, rendering population expansion primarily CD40-dependent (Fig. 4-5). However, BCR signaling provides an important modulatory role in T-dependent selection of B-cells. Chen et al. found BCR signaling to facilitate positive selection by prolonging B-cell survival and by priming B cells to receive synergistic Tfh cell signals (Chen *et al.*, 2023). What we found was consistent with this observation but completed with another part of the story: when costimulated with CD40, BCR signaling modulates the dose-response curve of CD40 by boosting less-stimulated cells with its pro-proliferative effects yet dampening proliferative responses of more-highly stimulated cells with its anti-survival effects (Fig. 3, 5). When stimulated alone, BCR regulates B-cell survival in a non-monotonic dose response curve, thereby potentially eliminating cells encoding self-reactive BCRs that elicit strong signals. Indeed, Shih et al. found both more cell division and increased cell death in higher-affinity B1-8$^{hi}$ B-cells compared to lower-affinity B1-8$^{lo}$ cells in

post-immunized mice spleen, highlighting again the paradoxical role of BCR stimulation (Shih, Roederer and Nussenzweig, 2002).

Considering the temporal dynamics of the process, our work delineated a narrow temporal window of opportunity for B-cells to receive CD40 signals following BCR activation. Proper timing (3hrs) of the two signals can maximize B-cell survival and proliferative response, while longer delays (8hrs) can lead to significant apoptosis and thus reduced population growth (Fig. 6). Consistent with this temporal window, Akkaya et al. also found that BCR signaling activated a metabolic program that imposed a limited time frame (9hrs) during which B-cells either receive a second signal (CD40 or CpG) or are eliminated due to mitochondrial dysfunction (Akkaya *et al.*, 2018). In contrast, Tan et al. showed that BCR-induced NR4A nuclear receptors were the key mediators of the restraint on B cell responses to antigen when the cell fails to receive signal 2 within a defined time window, by repressing MYC, and even T-cell chemokines (Tan *et al.*, 2020). Overall, regardless of the exact molecular mediator of the temporal window of opportunity, our model captured the phenotypes described in a large body of literature, and resolved apparently conflicting literature into a more unified systematic model.

Previous work that distinguished the phenotypes between naïve and GC B-cells often examined late GC B-cells 10-14 days after immunization (Luo, Weisel and Shlomchik, 2018). However, this strategy overlooked the early GC B-cells or the progression of the GC B-cell phenotype necessary for affinity-based selection under different dynamic range. In the early GC phase, where the average antigen-affinity is low, B-cells with mediocre-affinity BCRs need to survive and proliferate. On the other hand, in the late GC phase, where average antigen-affinity is high, the same B-cells with mediocre BCRs would need to avoid proliferating such that B-cells with the highest affinity could be distinguished appropriately. Competition among GC B-cells for antigens and T-cell-help contribute to this flexible dynamic range (Shih, Roederer and Nussenzweig, 2002). Here, we speculate about a phase-dependent dynamic range in antigen-affinity discrimination, where BCR-induced apoptosis and NFκB signaling saturation together tune the dose-dependent synergy and antagonism between BCR and CD40 signals. The integration of both signals sets a phase-dependent “timer” for B-cell selection. The timer can be further tuned through BCR-induced NFκB signaling, as previous literature suggested that late GC B-cells downregulate their BCR-induced NFκB activation compared to early activated B-cells (Young and Brink, 2021), indicating that remodeling of the BCR signaling network could also contribute to the phase-dependent dynamic range.

Consistent with opposing roles of BCR and CD40 signaling, previous work has suggested that variants that disrupted the signaling of either BCR and CD40 caused an imbalance of positive and negative selection and lead to immunodeficiency or autoimmune diseases. Specifically, Yam-Puc et al. found that enhanced BCR signaling through GC-B-cell-specific SHP-1 mutation led to early GC B-cell death, reducing antibody responses in mice (Yam-Puc *et al.*, 2021). On the other hand, enhanced CD40 signaling through TRAF3 mutations led to autoimmunity and increased risk of B-cell malignancy in humans (Rae *et al.*, 2022), while a lack of CD40 signaling through CD40L mutations led to immunodeficiency in humans (Kroczek *et al.*, 1994).

In summary, our findings may have implications not only for the maturation of high affinity antibodies but also for the escape of auto-reactive antibodies from negative selection as in autoimmunity. We speculate that the opposing roles of BCR and CD40 signals work together in determining B-cell fates, discriminating highly reactive B-cells as self- versus non-self may amount to a kinetic proofreading mechanism. Specifically, BCR ligand discrimination is due to two signaling steps (through BCR and CD40) that reduce the probability of generating unwanted antibodies. This increased specificity is obtained by introducing cell death, an irreversible step exiting the pathway that happens faster than the next step in the pathway, when the cell receives T-cell-help in the form of CD40 stimulation. Furthermore, this delay between ligand binding and B cell activation consumes free energy due to antigen processing and the activation of cell-death pathway. Understanding this process in greater detail may enable the design of vaccination protocols that maximize B-cell activation and proliferation while ensuring temporal dynamics that selectively induce apoptosis in unwanted B-cell clones, reducing risks of autoimmunity.

## Conflict of Interest Statement

The authors declare no conflict of interest.

## Author Contributions

HH undertook all mathematical modeling work and contributed to experiments. HVN led the experimental work. All authors contributed to the design of the study. AH secured funding and provided supervision. HH wrote the manuscript. All authors edited the manuscript.

## Acknowledgments

We thank current and former members of the Hoffmann lab for valuable discussions. We thank Xiaolu Guo, Sohyeon Park, Mark Xiang, and Aimilia Vareli for critical reading of the manuscript. AH acknowledges funding from sources R01AI132731 and R01AI127867. HVN acknowledges support from the James S McDonnell Foundation Postdoctoral Fellowship and the Damon Runyon Quantitative Biology Fellowship.

## REFERENCES

Akiyama, T., Shinzawa, M. and Akiyama, N. (2012) 'TNF receptor family signaling in the development and functions of medullary thymic epithelial cells', *Frontiers in immunology*, 3, p. 278. Available at: https://doi.org/10.3389/fimmu.2012.00278.

Akkaya, M. *et al.* (2018) 'Second signals rescue B cells from activation-induced mitochondrial dysfunction and death', *Nature Immunology*, 19(8), pp. 871–884. Available at: https://doi.org/10.1038/s41590-018-0156-5.

Bretscher, P. and Cohn, M. (1970) 'A Theory of Self-Nonself Discrimination', *Science*, 169(3950), pp. 1042–1049.

Burnet, M. (1957) 'Cancer—A Biological Approach', *British Medical Journal*, 1(5023), pp. 841–847.

Caldwell, A.B. *et al.* (2014) 'Network dynamics determine the autocrine and paracrine signaling functions of TNF', *Genes & Development*, 28(19), pp. 2120–2133. Available at: https://doi.org/10.1101/gad.244749.114.

606 Ceglia, V. *et al.* (2021) 'Anti-CD40 Antibodies Fused to CD40 Ligand Have Superagonist
607 Properties', *The Journal of Immunology*, 207(8), pp. 2060–2076. Available at:
608 https://doi.org/10.4049/jimmunol.2000704.
609 Chen, S.T. *et al.* (2023) 'B cell receptor signaling in germinal centers prolongs survival and
610 primes B cells for selection', *Immunity*, 56(3), pp. 547-561.e7. Available at:
611 https://doi.org/10.1016/j.immuni.2023.02.003.
612 Chen, W. *et al.* (1999) 'B Cell Apoptosis Triggered by Antigen Receptor Ligation Proceeds Via a
613 Novel Caspase-Dependent Pathway', *The Journal of Immunology*, 163(5), pp. 2483–2491.
614 Cheng, C.S. *et al.* (2017) 'Iterative Modeling Reveals Evidence of Sequential Transcriptional
615 Control Mechanisms', *Cell Systems*, 4(3), pp. 330-343.e5. Available at:
616 https://doi.org/10.1016/j.cels.2017.01.012.
617 Cheng, Z. *et al.* (2015) 'Distinct single-cell signaling characteristics are conferred by the MyD88
618 and TRIF pathways during TLR4 activation', *Science Signaling*, 8(385), p. ra69. Available at:
619 https://doi.org/10.1126/scisignal.aaa5208.
620 Coulter, E.M. *et al.* (2018) 'In vitro and in vivo evidence for uncoupling of B-cell receptor
621 internalization and signaling in chronic lymphocytic leukemia', *Haematologica*, 103(3), pp.
622 497–505. Available at: https://doi.org/10.3324/haematol.2017.176164.
623 Dadgostar, H. *et al.* (2002) 'Cooperation of multiple signaling pathways in CD40-regulated gene
624 expression in B lymphocytes', *Proceedings of the National Academy of Sciences*, 99(3), pp.
625 1497–1502. Available at: https://doi.org/10.1073/pnas.032665099.
626 Damdinsuren, B. *et al.* (2010) 'Single-round of antigen receptor signaling programs naïve B cells
627 to receive T cell help', *Immunity*, 32(3), pp. 355–366. Available at:
628 https://doi.org/10.1016/j.immuni.2010.02.013.
629 Dou, Z. *et al.* (2021) 'Aberrant Bcl-x splicing in cancer: from molecular mechanism to
630 therapeutic modulation', *Journal of Experimental & Clinical Cancer Research*, 40(1), p. 194.
631 Available at: https://doi.org/10.1186/s13046-021-02001-w.
632 Elgueta, R. *et al.* (2009) 'Molecular mechanism and function of CD40/CD40L engagement in the
633 immune system', *Immunological Reviews*, 229(1), pp. 152–172. Available at:
634 https://doi.org/10.1111/j.1600-065X.2009.00782.x.
635 Gao, Y., Kazama, H. and Yonehara, S. (2012) 'Bim regulates B-cell receptor-mediated
636 apoptosis in the presence of CD40 signaling in CD40-pre-activated splenic B cells
637 differentiating into plasma cells', *International Immunology*, 24(5), pp. 283–292. Available at:
638 https://doi.org/10.1093/intimm/dxr127.
639 Graves, J.D., Craxton, A. and Clark, E.A. (2004) 'Modulation and function of caspase pathways
640 in B lymphocytes', *Immunological Reviews*, 197(1), pp. 129–146. Available at:
641 https://doi.org/10.1111/j.0105-2896.2004.0110.x.
642 Hawkins, E.D. *et al.* (2013) 'Quantal and graded stimulation of B lymphocytes as alternative
643 strategies for regulating adaptive immune responses', *Nature Communications*, 4(1), p. 2406.
644 Available at: https://doi.org/10.1038/ncomms3406.
645 Inoue, K. *et al.* (2016) 'Oscillation dynamics underlie functional switching of NF-κB for B-cell
646 activation', *npj Systems Biology and Applications*, 2(1), pp. 1–9. Available at:
647 https://doi.org/10.1038/npjsba.2016.24.
648 Khalil, A.M., Cambier, J.C. and Shlomchik, M.J. (2012) 'B Cell Signal Transduction in Germinal
649 Center B Cells is Short-Circuited by Increased Phosphatase Activity', *Science (New York,
650 N.Y.)*, 336(6085), pp. 1178–1181. Available at: https://doi.org/10.1126/science.1213368.
651 Kroczek, R.A. *et al.* (1994) 'Defective expression of CD40 ligand on T cells causes "X-linked
652 immunodeficiency with hyper-IgM (HIGM1)"', *Immunological Reviews*, 138, pp. 39–59.
653 Available at: https://doi.org/10.1111/j.1600-065x.1994.tb00846.x.
654 Luo, W., Weisel, F. and Shlomchik, M.J. (2018) 'B Cell Receptor and CD40 Signaling Are
655 Rewired for Synergistic Induction of the c-Myc Transcription Factor in Germinal Center B

656 Cells', *Immunity*, 48(2), pp. 313-326.e5. Available at:
657 https://doi.org/10.1016/j.immuni.2018.01.008.
658 Mitchell, S. *et al.* (2018) 'Nongenetic origins of cell-to-cell variability in B lymphocyte
659 proliferation', *Proceedings of the National Academy of Sciences*, 115(12), pp. E2888–E2897.
660 Available at: https://doi.org/10.1073/pnas.1715639115.
661 Mitchell, S. *et al.* (2023) 'The NF-κB multidimer system model: A knowledge base to explore
662 diverse biological contexts', *Science Signaling*, 16(776), p. eabo2838. Available at:
663 https://doi.org/10.1126/scisignal.abo2838.
664 Nowosad, C.R., Spillane, K.M. and Tolar, P. (2016) 'Germinal center B cells recognize antigen
665 through a specialized immune synapse architecture', *Nature Immunology*, 17(7), pp. 870–
666 877. Available at: https://doi.org/10.1038/ni.3458.
667 Okada, T. *et al.* (2005) 'Antigen-Engaged B Cells Undergo Chemotaxis toward the T Zone and
668 Form Motile Conjugates with Helper T Cells', *PLOS Biology*, 3(6), p. e150. Available at:
669 https://doi.org/10.1371/journal.pbio.0030150.
670 Parker, D.C. (1993) 'T cell-dependent B cell activation', *Annual Review of Immunology*, 11, pp.
671 331–360. Available at: https://doi.org/10.1146/annurev.iy.11.040193.001555.
672 Qing, G., Qu, Z. and Xiao, G. (2005) 'Stabilization of Basally Translated NF-κB-inducing Kinase
673 (NIK) Protein Functions as a Molecular Switch of Processing of NF-κB2 p100*', *Journal of*
674 *Biological Chemistry*, 280(49), pp. 40578–40582. Available at:
675 https://doi.org/10.1074/jbc.M508776200.
676 Rae, W. *et al.* (2022) 'Immunodeficiency, autoimmunity, and increased risk of B cell malignancy
677 in humans with TRAF3 mutations', *Science Immunology*, 7(74), p. eabn3800. Available at:
678 https://doi.org/10.1126/sciimmunol.abn3800.
679 Rodriguez, B.N. *et al.* (2024) 'The noncanonical NFκB pathway: Regulatory mechanisms in
680 health and disease', *WIREs Mechanisms of Disease*, n/a(n/a), p. e1646. Available at:
681 https://doi.org/10.1002/wsbm.1646.
682 Roederer, M. (2011) 'Interpretation of cellular proliferation data: Avoid the panglossian',
683 *Cytometry Part A*, 79A(2), pp. 95–101. Available at: https://doi.org/10.1002/cyto.a.21010.
684 Roy, K. *et al.* (2019) 'A Regulatory Circuit Controlling the Dynamics of NFκB cRel Transitions B
685 Cells from Proliferation to Plasma Cell Differentiation', *Immunity*, 50(3), pp. 616-628.e6.
686 Available at: https://doi.org/10.1016/j.immuni.2019.02.004.
687 Rush, J.S. and Hodgkin, P.D. (2001) 'B cells activated via CD40 and IL-4 undergo a division
688 burst but require continued stimulation to maintain division, survival and differentiation',
689 *European Journal of Immunology*, 31(4), pp. 1150–1159. Available at:
690 https://doi.org/10.1002/1521-4141(200104)31:4<1150::AID-IMMU1150>3.0.CO;2-V.
691 Sen, R. (2006) 'Control of B Lymphocyte Apoptosis by the Transcription Factor NF-κB',
692 *Immunity*, 25(6), pp. 871–883. Available at: https://doi.org/10.1016/j.immuni.2006.12.003.
693 Shih, T.-A.Y., Roederer, M. and Nussenzweig, M.C. (2002) 'Role of antigen receptor affinity in T
694 cell–independent antibody responses in vivo', *Nature Immunology*, 3(4), pp. 399–406.
695 Available at: https://doi.org/10.1038/ni776.
696 Shinohara, H. *et al.* (2014) 'Positive Feedback Within a Kinase Signaling Complex Functions as
697 a Switch Mechanism for NF-κB Activation', *Science*, 344(6185), pp. 760–764. Available at:
698 https://doi.org/10.1126/science.1250020.
699 Shinohara, H. *et al.* (2016) 'Stimulus-Dependent Inhibitor of Apoptosis Protein Expression
700 Prolongs the Duration of B Cell Signalling', *Scientific Reports*, 6(1), p. 27706. Available at:
701 https://doi.org/10.1038/srep27706.
702 Shokhirev, M.N. *et al.* (2015) 'A multi-scale approach reveals that NF-κB cR el enforces a B-cell
703 decision to divide', *Molecular Systems Biology*, 11(2), p. 783. Available at:
704 https://doi.org/10.15252/msb.20145554.

Shokhirev, M.N. and Hoffmann, A. (2013) 'FlowMax: A Computational Tool for Maximum Likelihood Deconvolution of CFSE Time Courses', *PLOS ONE*, 8(6), p. e67620. Available at: https://doi.org/10.1371/journal.pone.0067620.

Shulman, Z. *et al.* (2014) 'Dynamic signaling by T follicular helper cells during germinal center B cell selection', *Science*, 345(6200), pp. 1058–1062. Available at: https://doi.org/10.1126/science.1257861.

Silva, M. *et al.* (2017) 'Targeted Elimination of Immunodominant B Cells Drives the Germinal Center Reaction toward Subdominant Epitopes', *Cell reports*, 21(13), pp. 3672–3680. Available at: https://doi.org/10.1016/j.celrep.2017.12.014.

Tan, C. *et al.* (2020) 'NR4A nuclear receptors restrain B cell responses to antigen when second signals are absent or limiting', *Nature Immunology*, 21(10), pp. 1267–1279. Available at: https://doi.org/10.1038/s41590-020-0765-7.

Tucker, T.A. and Schwiebert, L.M. (2008) 'CD40 ligation decreases its protein half-life at the cell surface', *European Journal of Immunology*, 38(3), pp. 864–869. Available at: https://doi.org/10.1002/eji.200737828.

Turner, M.L., Hawkins, E.D. and Hodgkin, P.D. (2008) 'Quantitative Regulation of B Cell Division Destiny by Signal Strength', *The Journal of Immunology*, 181(1), pp. 374–382. Available at: https://doi.org/10.4049/jimmunol.181.1.374.

Victora, G.D. *et al.* (2010) 'Germinal Center Dynamics Revealed by Multiphoton Microscopy with a Photoactivatable Fluorescent Reporter', *Cell*, 143(4), pp. 592–605. Available at: https://doi.org/10.1016/j.cell.2010.10.032.

Victora, G.D. and Nussenzweig, M.C. (2022) 'Germinal Centers', *Annual Review of Immunology*, 40(1), p. null. Available at: https://doi.org/10.1146/annurev-immunol-120419-022408.

Yam-Puc, J.C. *et al.* (2021) 'Enhanced BCR signaling inflicts early plasmablast and germinal center B cell death', *iScience*, 24(2), p. 102038. Available at: https://doi.org/10.1016/j.isci.2021.102038.

Young, C. and Brink, R. (2021) 'The unique biology of germinal center B cells', *Immunity*, 54(8), pp. 1652–1664. Available at: https://doi.org/10.1016/j.immuni.2021.07.015.

Zhao, K. *et al.* (2016) 'Intracellular osteopontin stabilizes TRAF3 to positively regulate innate antiviral response', *Scientific Reports*, 6, p. 23771. Available at: https://doi.org/10.1038/srep23771.

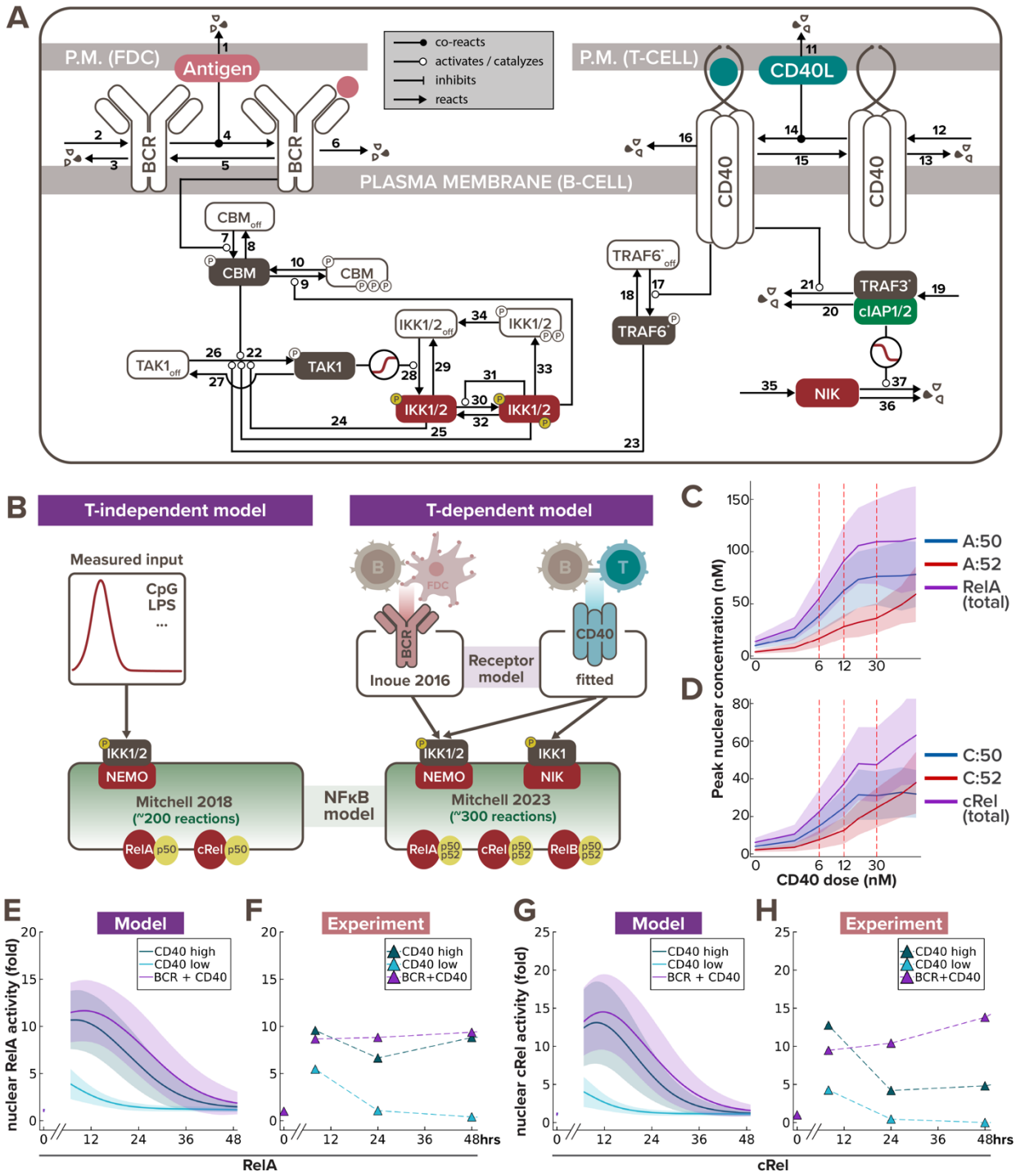


**Figure 1. Multi-scale model recapitulates B-cell NFκB dynamics in response to T-dependent stimulation.**

**(A)** Schematic of BCR-CD40 receptor model to recapitulate T-dependent activation of B-cells. **(B)** Schematics of existing T-independent (left) and newly integrated T-dependent (right) NFκB signaling modeling frameworks. T-independent stimulation typically only involves a single ligand (e.g. CpG or LPS), while T-dependent stimulation always involve a more complex receptor signaling system of both BCR and CD40 ligands. Low, medium and high dose of CD40 were set to 6nM, 12nM, and 30nM, respectively, to correspond to the three experimental doses we used

(1μg/mL, 3.3μg/mL, and 10μg/mL). **(C-D)** Line graph from model simulations show **(C)** peak nuclear RelA and **(D)** peak nuclear cRel levels in response to increasing CD40 doses, where the shading represents the sample standard deviation of 1000 cells. X-axes are plotted on a log-scale to accommodate a wide range of concentrations. **(E)** Line graphs from model simulations of 1000 virtual cells and **(F)** matching experiments with 600K founder B-cells show temporal trajectories of nuclear RelA level at 0, 7, 24, and 48hrs following stimulation with low α-CD40 (1μg/mL), high α-CD40 (10μg/mL), or costimulation with high α-CD40 and α-BCR (10μg/mL each). Darker colored lines represent the average nuclear RelA level from 1000 cells and the lighter shading represents the sample standard deviation of the 1000 cells. **(G-H)** Line graphs of nuclear cRel level in matching stimulation conditions as (E-F).

**Table 1. Model reactions and parameter values**

| Module | # | Reactions | Rates | Units | Source |
|---|---|---|---|---|---|
| BCR receptor | 1 | ANTIGEN → | 0.05 | hr-1 | fitted (antibody) |
| | 2 | → BCR | 4.93 | nM hr-1 | fitted |
| | 3 | BCR → | 1.43 | hr-1 | fitted |
| | 4 | ANTIGEN + BCR → ABCR | 66 | nM-1 hr-1 | fitted |
| | 5 | ABCR → ANTIGEN + BCR | 1.26 | hr-1 | fitted |
| | 6 | ABCR → | 0.35 | hr-1 | Coulter et al 2018 |
| | 7 | CBM + ABCR → ACBM + ABCR | 6.6 | nM-1 hr-1 | Inoue et al 2016 |
| | 8 | ACBM → CBM | 0.126 | hr-1 | Inoue et al 2016 |
| | 9 | ACBM + IKK → ICBM + IKK | 0.181 | nM-1 hr-1 | Inoue et al 2016 |
| | 10 | ICBM → CBM | 0.068 | hr-1 | Inoue et al 2016 |
| CD40 receptor | 11 | CD40L → | 0.05 | hr-1 | fitted (antibody) |
| | 12 | → CD40R | 7.672 | nM hr-1 | fitted |
| | 13 | CD40R → | 0.05 | hr-1 | Tucker et al 2008 |
| | 14 | CD40L + CD40R → CD40LR | 0.04 | nM-1 hr-1 | Ceglia et al 2021 |
| | 15 | CD40LR → CD40L + CD40R | 11.3 | hr-1 | Ceglia et al 2021 |
| | 16 | CD40LR → | 0.17 | hr-1 | Tucker et al 2008 |
| | 17 | CD40LR + $TRAF6_{OFF}$ → CD40LR + TRAF6 | 0.1 | nM-1 hr-1 | Cheng et al 2015 |
| | 18 | TRAF6 → $TRAF6_{OFF}$ | 7.5 | hr-1 | Cheng et al 2015 |
| | 19 | → TRAF3 | 10 | nM hr-1 | fitted |
| | 20 | TRAF3 → | 0.5 | hr-1 | Zhao et al 2016 |
| | 21 | CD40LR + TRAF3 → CD40LR | 10 | nM-1 hr-1 | fitted |
| TAK1 dynamics | 22 | ACBM + TAK1 → ACBM + ATAK1 | 1050 | nM-1 hr-1 | Shinohara et al 2014 |
| | 23 | TRAF6 + TAK1 → TRAF6 + ATAK1 | 60 | nM-1 hr-1 | Cheng et al 2015 |
| | 24 | IKK2 + TAK1 → IKK2 + ATAK1 | 401.14 | nM-1 hr-1 | Shinohara et al 2014 |
| | 25 | IKK3 + TAK1 → IKK3 + ATAK1 | 1182.86 | nM-1 hr-1 | Shinohara et al 2014 |
| | 26 | TAK1 → ATAK1 | 249 | hr-1 | Shinohara et al 2014 |
| | 27 | ATAK1 → TAK1 | 258600 | hr-1 | Shinohara et al 2014 |
| IKK dynamics | 28 | TAK1 + IKK_OFF → TAK1 + IKK2 | 80.72 | hr-1 | Shinohara et al 2016 |
| | 29 | IKK2 → IKK_OFF | 2175.6 | hr-1 | Shinohara et al 2016 |
| | 30 | IKK2 → IKK3 | 0.009 | hr-1 | Shinohara et al 2016 |
| | 31 | IKK3 + IKK2 → IKK3 + IKK3 | 2094 | hr-1 | Shinohara et al 2016 |
| | 32 | IKK3 → IKK2 | 53844 | hr-1 | Shinohara et al 2016 |
| | 33 | IKK3 → IIKK | 2528.4 | hr-1 | Shinohara et al 2016 |
| | 34 | IIKK → IKK_OFF | 957.6 | hr-1 | Shinohara et al 2016 |
| NIK dynamics | 35 | → NIK | 12 | nM hr-1 | Mitchell et al 2023 |
| | 36 | NIK → | 0.231 | hr-1 | Mitchell et al 2023 |
| | 37 | TRAF3 + NIK → TRAF3 | 2 | nM-1 hr-1 | Qing et al 2005 |

(Qing, Qu and Xiao, 2005; Tucker and Schwiebert, 2008; Shinohara *et al.*, 2014, 2016; Cheng *et al.*, 2015; Inoue *et al.*, 2016; Zhao *et al.*, 2016; Coulter *et al.*, 2018; Ceglia *et al.*, 2021; Mitchell *et al.*, 2023)

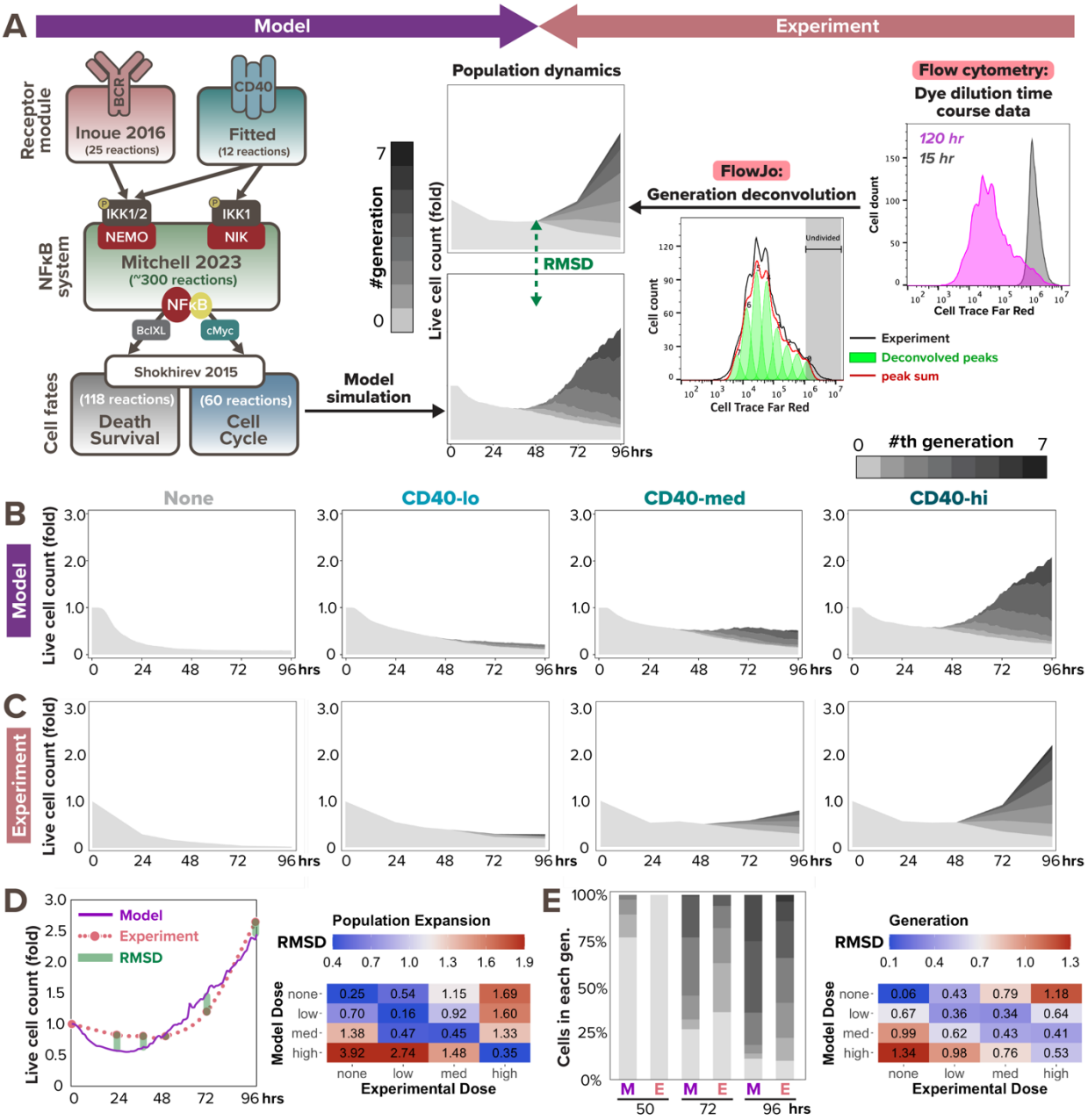


**Figure 2. Multi-scale model recapitulates B-cell population dynamics in response to CD40 stimulation.**

**(A)** Workflow of fitting model simulations to experimental B-cell population dynamics following stimulation. Left: schematic of full T-dependent modeling framework. Right: experimental workflow with Cell Trace Far Red (CTFR) dye dilution. **(B)** Stacked area plots from model simulations of 1000 virtual B-cells show their population dynamics in response to stimulation with (from left to right) no (0nM), low (6nM), medium (12nM), and high (30nM) dose of α-CD40. Each subsequent generation of proliferating cells is indicated with a darker gray. **(C)** Stacked area plots from matching experiments of 19196 founder B-cells show their population dynamics in response to no (0μg/mL), low (1μg/mL), medium (3.3μg/mL), or high (10μg/mL) dose of α-CD40. **(D-E)** Root mean square deviation (RMSD) is calculated between simulated and experimental data, and is composed of 2 scores: RMSD of **(D)** relative population size expansion and RMSD of **(E)** generation composition. An example of RMSD between model and

778 experimental data is shown on the left side of (D) and (E), and a heatmap of the RMSD scores
779 in matching (diagonal) or mismatching (off-diagonal) model-and-experiment pairs is shown on
780 the right side. Lower RMSD scores correspond to better fit.

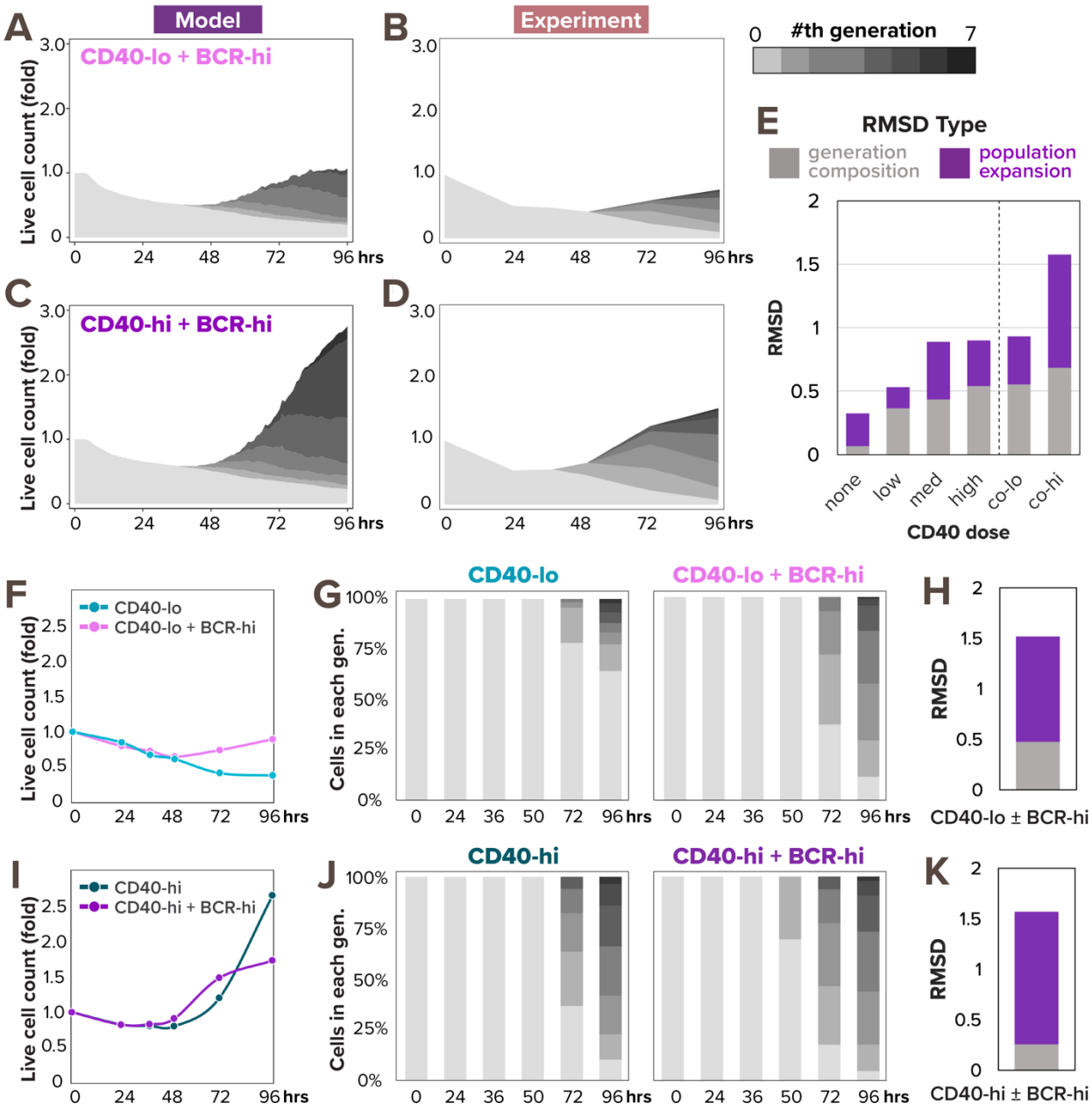


**Figure 3. Model predicts synergistic population expansion in response to BCR and CD40 costimulation, but experiment reveals dose-dependent interaction between the stimuli.** **(A)** Stacked area plot from model simulations of 1000 virtual B-cells show their population dynamics in response to costimulation with high α-IgM (0.25nM) and low α-CD40 (6nM). Each subsequent generation of proliferating cells is indicated with a darker gray. **(B)** Stacked area plot from matching experiments of 19196 founder B-cells show their population dynamics in response to high α-IgM (10μg/mL) and low α-CD40 (1μg/mL) costimulation. **(C)** Stacked area plot from model simulations of 1000 virtual B-cells show their population dynamics in response to costimulation with high α-IgM (0.25nM) and high α-CD40 (30nM). **(D)** Stacked area plot from matching experiments of 19196 founder B-cells show their population dynamics in response to high α-IgM (10μg/mL) and high α-CD40 (10μg/mL) costimulation. **(E)** Stacked bar graph shows a breakdown of total RMSD by types in the 2 costimulation conditions compared to the 4 model-and-experiment pairs in Fig. 2B-C which includes no, low, medium, and high dose of CD40. **(F)**

Line graph of experimental population expansion index is higher in response to costimulation than without α-IgM. **(G)** Stacked bar graph of experimental generation composition dynamics in response to low α-CD40 stimulation with or without high α-IgM costimulation. **(H)** Stacked bar graph of RMSD score between the 2 experimental conditions in (G) shows the addition of high α-IgM changes both population expansion and generation composition. **(I)** Line graph of experimental population expansion index is lower in response to costimulation than without α-IgM. **(J)** Stacked bar graph of experimental generation composition dynamics in response to high α-CD40 stimulation with high α-IgM costimulation. **(K)** Stacked bar graph of RMSD score between the 2 experimental conditions in (J) shows the addition of high α-IgM predominantly affects population expansion.

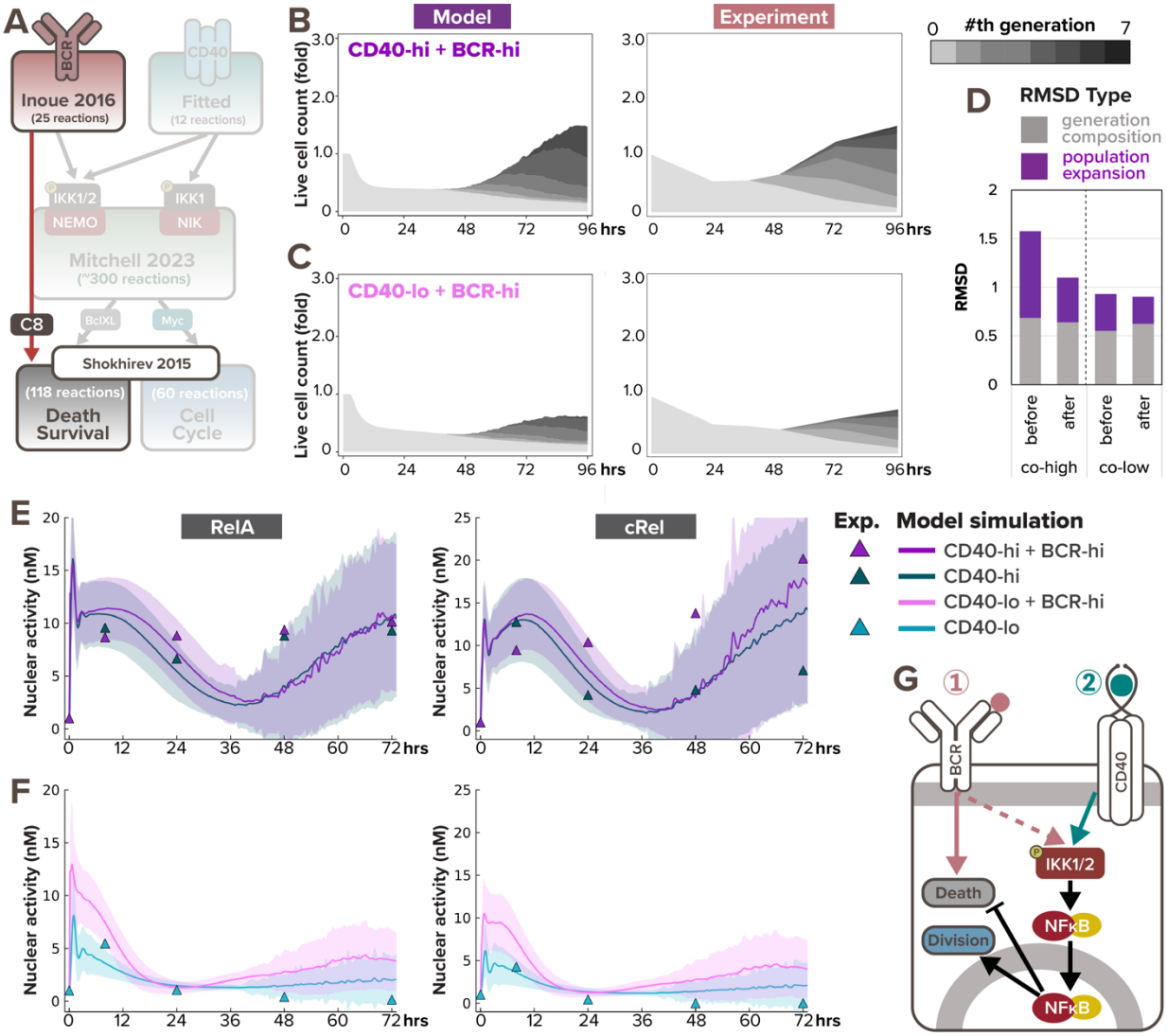


**Figure 4. BCR-induced caspase-dependent apoptosis and NFκB signaling saturation explains the dose-dependent interaction in costimulation.**

**(A)** Schematic of updated T-dependent multi-scale B-cell model where activated BCR induces caspase-8 processing. **(B)** Stacked area plots from model simulation and matching experiment show B-cell population dynamics in response to costimulation with high α-IgM (0.25nM and 10μg/mL) and high α-CD40 (30nM and 10μg/mL) with the addition of BCR-induced caspase processing. Each subsequent generation of proliferating cells is indicated with a darker gray. **(C)** Stacked area plots from model simulation and matching experiment show B-cell population dynamics in response to costimulation with high α-IgM (0.25nM and 10μg/mL) and low α-CD40 (6nM and 1μg/mL) with the addition of BCR-induced caspase processing. **(D)** Bar graph of total RMSDs of the 2 costimulation conditions after the addition of BCR-induced caspase processing compared with before the addition. **(E-F)** Model simulations (lines) and immunoblot quantification (triangles) show consistent average nuclear RelA and cRel level in naïve B-cells costimulated with **(E)** high α-CD40 and high α-IgM or **(F)** low α-CD40 and high α-IgM at 0, 7, 24, 48hrs, and 72hrs since stimulation onset. Darker colored lines represent average nuclear RelA level from cells that are alive at the timepoint, whereas the shading represents the sample standard deviation of the cells. **(G)** Schematic of BCR stimulation being pro-proliferative and anti-apoptotic due to NFκB signaling yet pro-apoptotic due to AICD.

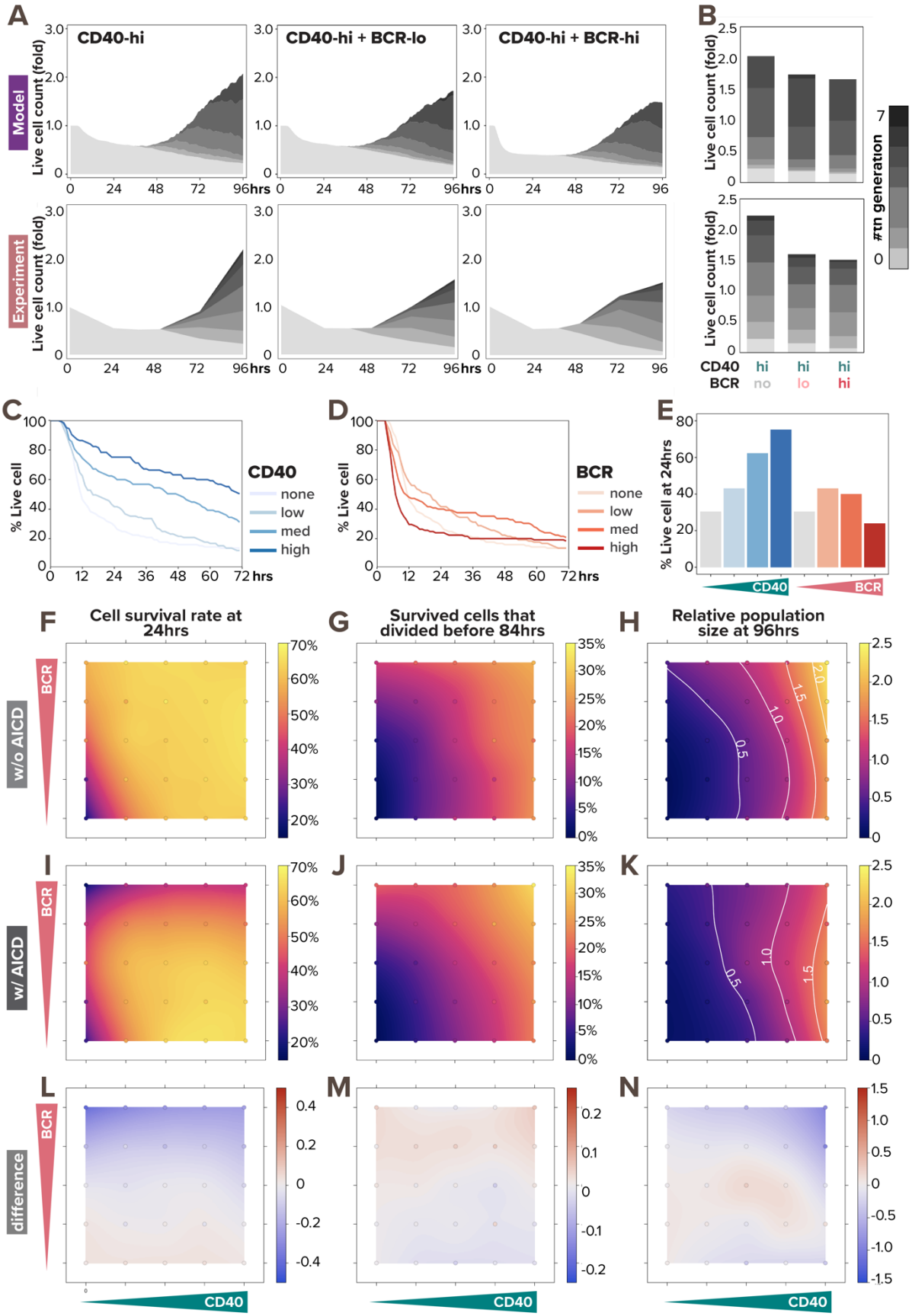


825

826 **Figure 5. BCR-induced apoptosis prevents BCR stimulation from promoting population**
827 **growth. (A)** Stacked area plots from model simulations of 1000 virtual B-cells (top) and
828 matching experiments of 19196 founder B-cells (bottom) show their population dynamics in
829 response to costimulation with high (30nM and 10μg/mL) α-CD40 and no (0nM and 0μg/mL),
830 low (0.005nM and 1μg/mL), or high (0.25nM and 10μg/mL) dose of α-BCR under the impact of
831 AICD. Each subsequent generation of proliferating cells is indicated with a darker gray. **(B)**
832 Stacked bar graph from model simulations (top) and experiments (bottom) show a breakdown of
833 live B-cells by generation numbers at 96hrs post-stimulation-onset. **(C-D)** Model-simulated
834 Kaplan-Meier survival curve in response to **(C)** α-CD40 dose and **(D)** α-BCR dose shows
835 distinct pattern regarding monotonicity. **(E)** Bar graph from model simulations show percentage
836 live B-cells at 24hrs in response to increasing α-CD40 and α-BCR doses. **(F-K)** Heatmaps from
837 model simulations of 1000 virtual B-cells in response to 25 single- or co-stimulation scenarios
838 (with 5 doses of α-CD40: 0, 6, 12, 18, and 30nM, and 5 doses of α-BCR: 0, 0.0005, 0.005, 0.05,
839 and 0.25nM, combinatorially) show the percentage of survived B-cells at 24 hours under **(F)** no
840 AICD and **(I)** with AICD, the percentage of proliferative B-cells by 84hrs out of those that
841 survived **(G)** without AICD and **(J)** with AICD, and the relative population size at 96hrs
842 (normalized to founder cell population size) **(H)** without AICD and **(K)** with AICD, where white
843 contour lines represent 0.5-, 1.0-, 1.5-, and 2.0-fold changes. **(L)** Heatmap shows the
844 differences between (F) and (I). **(M)** Heatmap shows the differences between (G) and (J). **(N)**
845 Heatmap shows the differences between (H) and (K). In (F-N), the 25 simulated doses are
846 plotted as colored circles in a scatterplot, whereas the space in between doses is interpolated
847 with a locally estimated scatterplot smoothing (LOESS) curve.
848
849

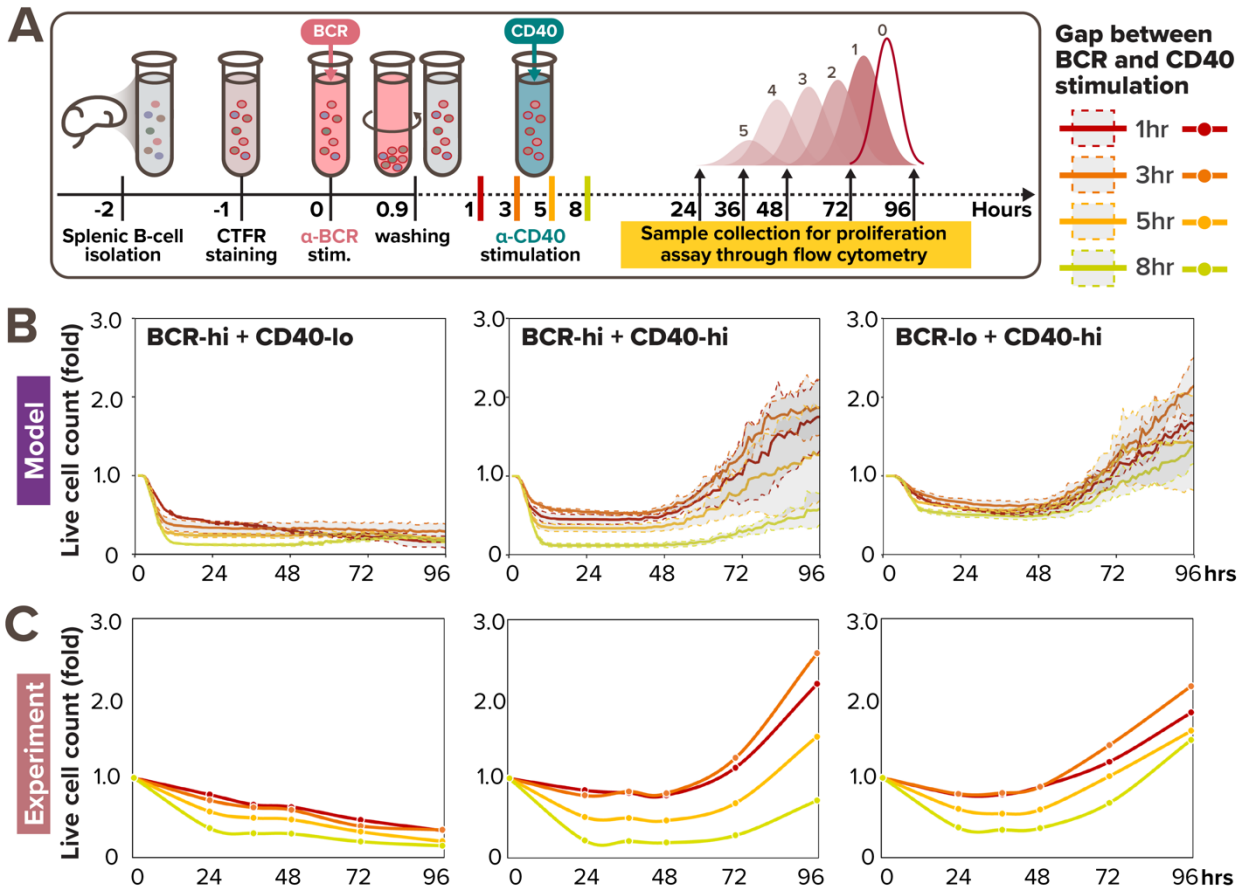


**Figure 6. Sequential BCR-CD40 simulation reveals a limited window of opportunity to acquire CD40 signal.**

**(A)** *In vitro* experimental workflow where primary B cells are sequentially stimulated with pulsing α-BCR, followed by α-CD40 stimulation 1, 3, 5, or 8hrs later. **(B)** Line graph from model simulations of 1000 virtual B-cells show their population expansion in response to sequential costimulation with high BCR (0.25nM) and low CD40 (6nM) (left), high BCR (0.25nM) and high CD40 (30nM) (middle), and low BCR (0.005nM) and high CD40 (30nM) (right), colored by the gap between BCR and CD40 stimulation. Each thick colored line represents the average population expansion from 1000 cells, and the shading represents the population standard deviation from the 8 simulations, each with 125 founder cells. **(C)** Line graph from matching experiments of 19196 founder B-cells show their population expansion in response to sequential costimulation with high BCR (10μg/mL) and low CD40 (1μg/mL) (left), high BCR (10μg/mL) and high CD40 (10μg/mL) (middle), and low BCR (1μg/mL) and high CD40 (10μg/mL) (right), colored by the gap between BCR and CD40 stimulation.

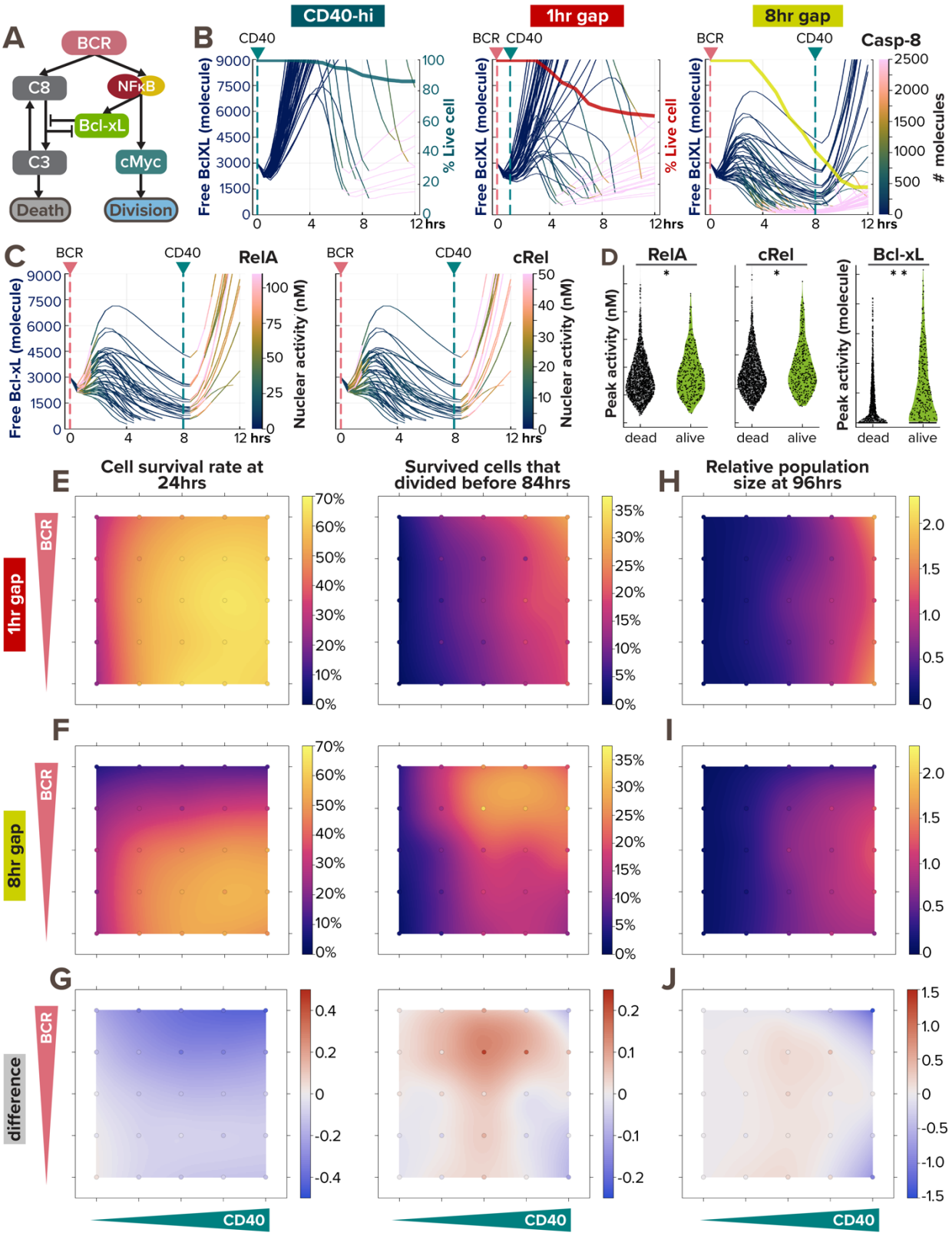


**Figure 7. BCR-induced anti-apoptotic BclXL protects cells from dying from AICD, as a form of paradoxical signaling.**

**(A)** Schematic of paradoxical BCR signaling that promotes proliferation, survival, and death of

B-cells through cMyc, Bcl-xL, and caspase-8, respectively. **(B)** Line plots of Bcl-xL activity (left axis) colored by caspase-8 level (color bar) in 50 model-simulated single-cells show the correlation between Bcl-xL consumption and caspase-8 activity. The thick line overlaid on top is a Kaplan-Meier survival curve (right axis). The pink and green vertical dashed lines represent the timing of BCR and CD40 stimulation, respectively. From left to right, the 3 conditions are: high α-CD40 costimulation, and sequential α-BCR and α-CD40 stimulation with a 1hr and 8hr gap. When a cell dies, the line continues (and becomes pink due to high caspase-8 level). **(C)** Line plots of Bcl-xL activity colored by RelA (left) and cRel (right) activity in 50 model-simulated single-cells demonstrate the correlation between NFκB activation and BclXL upregulation in B-cells costimulated sequentially with an 8hr gap. When a cell dies, the line discontinues. **(D)** Violin plot of peak RelA, cRel, and Bcl-xL activity in 2000 model-simulated B-cells in response to sequential costimulated with an 8hr gap show the differences between cells that died within the first 12 hours and those that survived. Statistical significance is evaluated using a Mann Whitney U test, with p-values of 0.0019, 0.0077, and <1e-18, correspondingly. **(E-J)** Heatmaps from model simulations of 1000 virtual B-cells in response to 25 single or costimulation scenarios (with 5 doses of α-CD40: 0, 6, 12, 18, and 30nM, and 5 doses of α-BCR: 0, 0.0005, 0.005, 0.05, and 0.25nM, combinatorially) show the percentage of survived cell at 24 hours after stimulation onset (left) and the percentage of survived cells that proliferated by 84hrs (right) in **(E)** 1hr sequential costimulation or **(F)** 8hr sequential costimulation. **(G)** Heatmap highlights the difference between (E) and (F). **(H-I)** Heatmap of relative population size at 96hrs between **(H)** 1hr sequential stimulation and **(I)** 8hr sequential stimulation shows the biggest difference **(J)** in the upper right and lower right corners. In (E-J), the 25 simulated doses are plotted as colored circles in a scatterplot, whereas the space in between doses is interpolated with a locally estimated scatterplot smoothing (LOESS) curve.

## SUPPLEMENTAL MATERIALS: Supplemental Figures and Materials and Methods

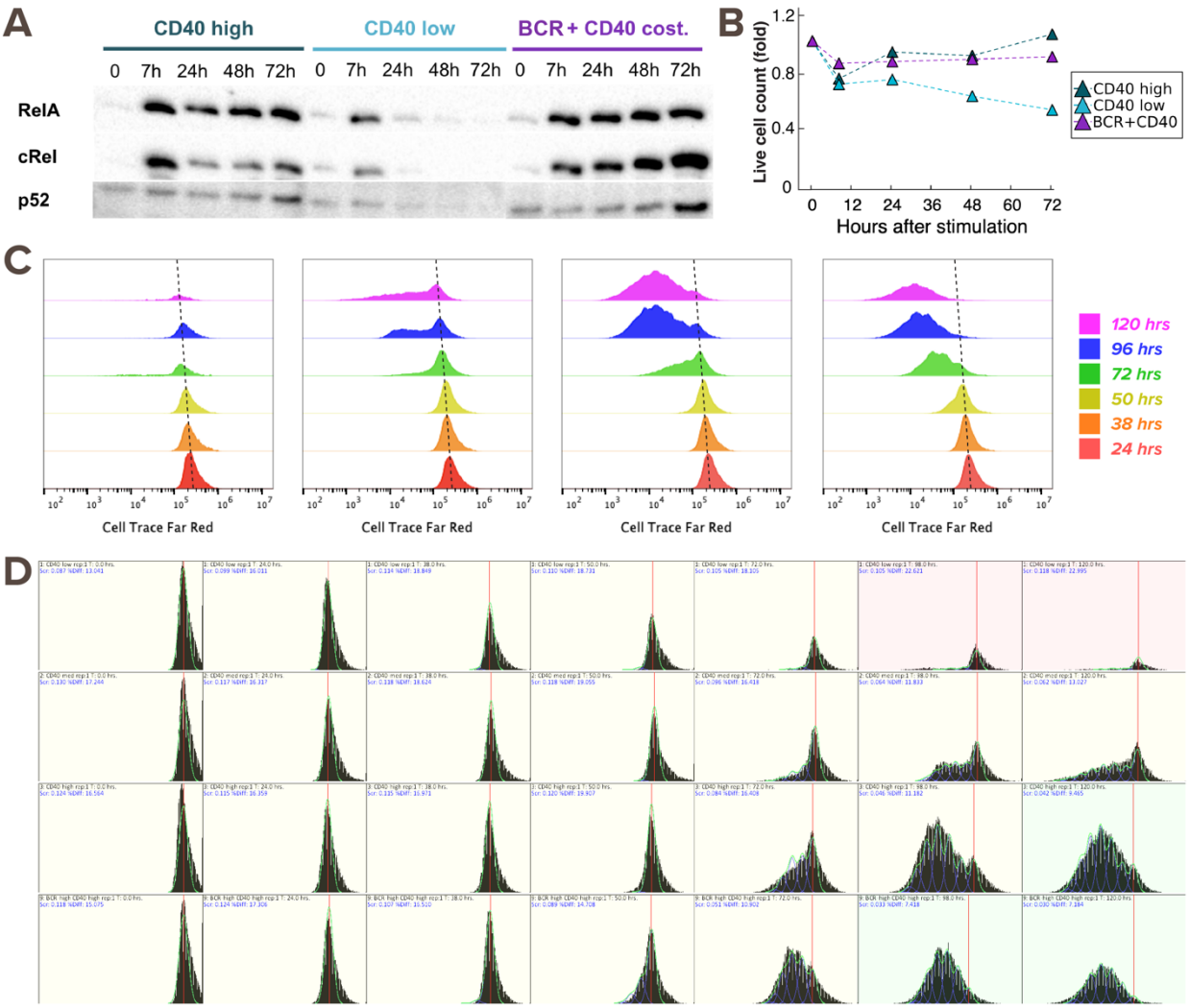


**Figure S1. Raw experimental data to test the multi-scale B-cell model. (A)** Immunoblot from experiments with 600K founder B-cells show nuclear RelA, cRel, and p52 levels at 0, 7, 24, 48, and 72hrs after stimulation with low α-CD40 (1μg/mL), high α-CD40 (10μg/mL), or costimulation with high α-CD40 and α-IgM (10μg/mL) . **(B)** Line graph of live B-cell count (fold-change) for each timepoint in (A), to which the samples are adjusted when loading to the gel. The cell count fluctuation is due to cell death, cell division, and technical error when transferring cells. **(C)** Cell Trace Far Red (CTFR) dye dilution fluorescence histogram for B-cells stimulated with (from left to right) low (1μg/mL), medium (3.3μg/mL), and high (10μg/mL) dose of α-CD40 and costimulation of high α-CD40 and α-IgM (10μg/mL). There is a baseline shift in CTFR fluorescence by about 2-fold from 24hrs to 120hrs (dotted line), which we adjusted when deconvolving the cells into each generation. **(D)** Deconvolution of the time courses in (C) into each generation, where the red line indicates the center of the undivided population of cells, the blue lines indicate individual proliferation peaks, and the green line represents the model sum.

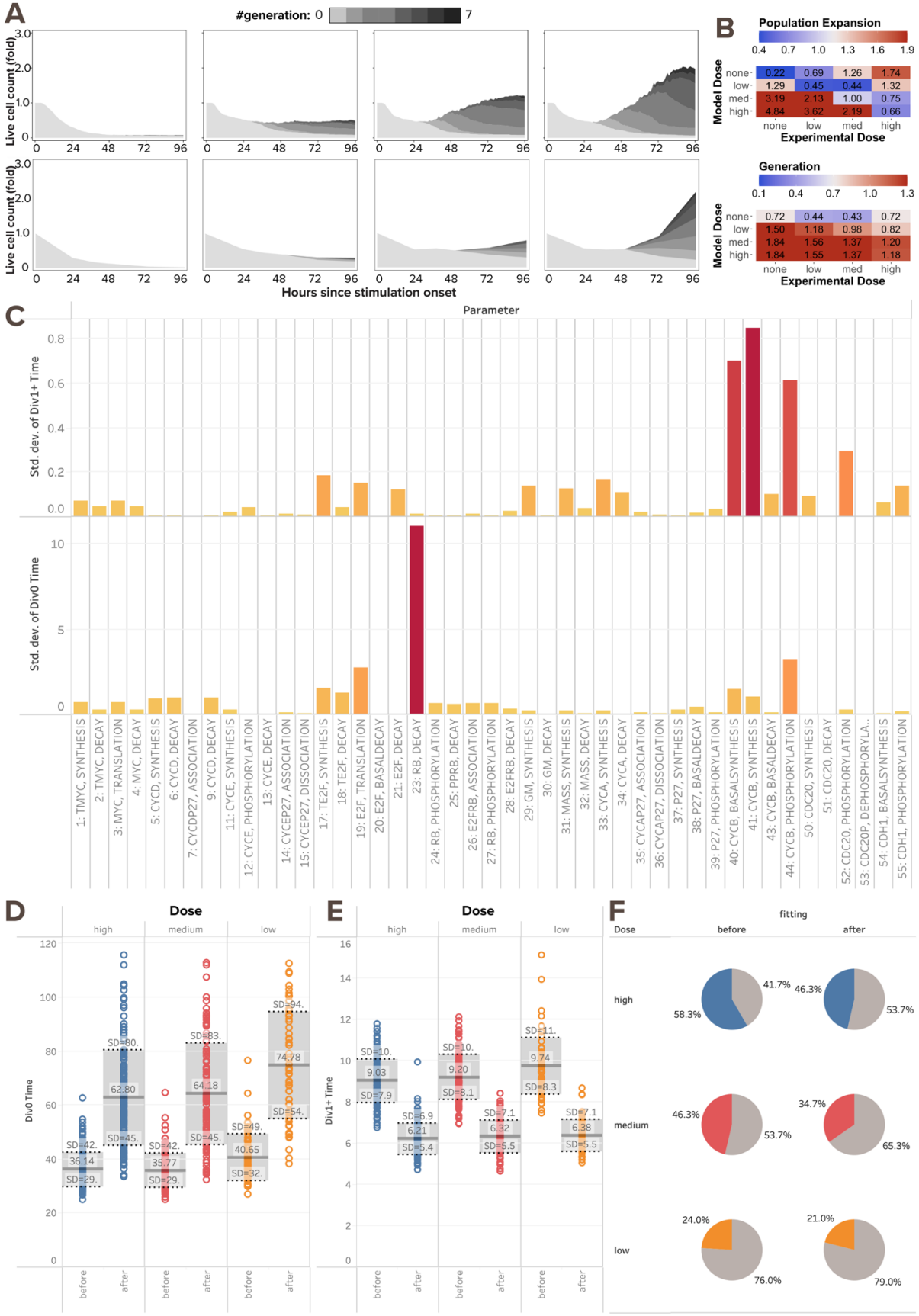


913

**Figure S2. Multi-scale model needs tuning to recapitulate B-cell population dynamics in response to CD40 stimulation.**
**(A)** Stacked area plots from model simulations of 1000 virtual B-cells (top) and matching experiments with 19196 founder B-cells (bottom) show their population dynamics in response to stimulation with (from left to right) no (0nM and 0μg/mL), low (6nM and 1μg/mL), medium (12nM and 3.3μg/mL), and high (30nM and 10μg/mL) dose of α-CD40. Each subsequent generation of proliferating cells is indicated with a darker gray. **(B)** Heatmap shows RMSD of relative population size expansion (top) and generation composition (bottom) in matching (diagonal) or mismatching (off-diagonal) model-and-experiment pairs. Some model doses (medium and low) are more deviated from their matching than mismatching experimental doses (high and medium, respectively), indicating a subpar fit. **(C)** Bar graph from local sensitivity analysis of parameters in the cell cycle module shows their standard deviations in time to first division (Tdiv0) and time to later divisions (Tdiv1+). Local sensitivity analysis is achieved by repetitive simulations that independently scaling each parameter in the cell cycle module by 0.2, 0.33, 0.4, 0.5, 0.66, 1.0, 1.5, 2.0, 2.5, 3.0, or 5.0-fold. 2 out of 55 parameters stand out as the best candidates for tuning Tdiv0 and Tdiv1+: retinoblastoma (Rb) decay rate and cyclin B (CycB) synthesis rate, respectively. These parameters were tuned in order to achieve a later and more dose-responsive Tdiv0, shorter Tdiv1+, and smaller divider percentage. **(D)** Box plots from model simulations of 300 virtual B-cells show the mean Tdiv0 increases for all doses after parameter tuning. **(E)** Box plots from model simulations of 300 virtual B-cells show the mean Tdiv1+ decreases for all doses after parameter tuning. **(F)** Pie charts from model simulations of 300 virtual B-cells show the percentage of dividing cells (colored slices) out of all founder cells decreases for all doses, while maintaining CD40 dose-responsiveness. Grey slices are the non-dividing founder cells that either die or survive without division.

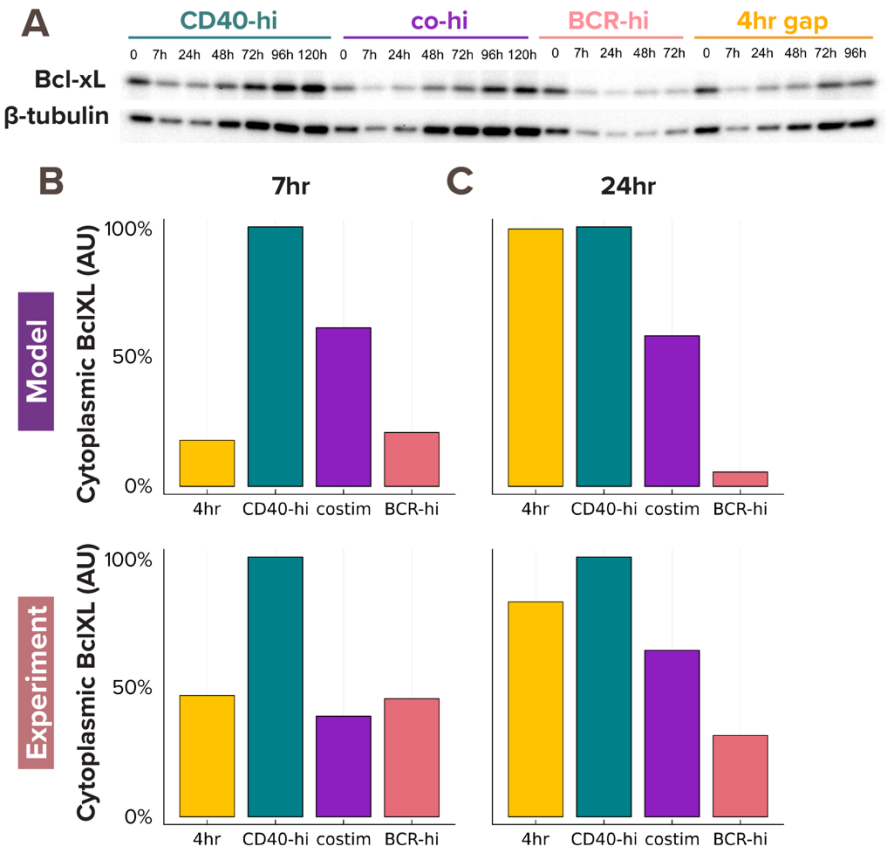


**Figure S3. Model-simulated cytoplasmic BclXL level recapitulates experimental results.** **(A)** Immunoblot from experiments with 600K founder B-cells show cytoplasmic Bcl-xL and β-tubulin levels in response to stimulation with (from left to right) high (10μg/mL) dose of α-CD40, high α-CD40 and high α-BCR, high α-BCR, and sequential stimulation of high α-BCR and high α-BCR with a 4hr delay. **(B-C)** Bar graphs from model simulations (top) and experiments (bottom) show consistent max-normalized quantification of cytoplasmic Bcl-xL level at **(B)** 7hrs and **(C)** 24hrs.

949 **MATERIALS AND METHODS**
950
951
952 **Key Resources Table**

| REAGENT or RESOURCE | SOURCE | IDENTIFIER |
|---|---|---|
| **Antibodies** | | |
| Rabbit polyclonal anti-RelA | Santa Cruz Biotechnologies | sc-372; RRID: AB_632037 |
| Rabbit polyclonal anti-cRel | Santa Cruz Biotechnologies | sc-71; RRID: AB_2253705 |
| Rabbit polyclonal anti-p50 | Santa Cruz Biotechnologies | sc-114; RRID: AB_632034 |
| Mouse monoclonal anti-Bcl-xL | Santa Cruz Biotechnologies | sc-8392; RRID: AB_626739 |
| Rabbit polyclonal anti-p84 | Abcam | ab131268 |
| Mouse monoclonal anti-β-tubulin | Sigma Aldrich | T5201; RRID: AB_609915 |
| HRP Anti-mouse secondary | Cell Signaling Technology | 7076; RRID: AB_330924 |
| HRP Anti-rabbit secondary | Cell Signaling Technology | 7074; RRID: AB_2099233 |
| CD40 monoclonal antibody (IC10) | Invitrogen | 16-0401-86; RRID: AB_468940 |
| Goat anti-mouse IgM | Jackson ImmunoResearch | 115-066-020; RRID: AB_2338579 |
| **Chemicals, Peptides, and Recombinant Proteins** | | |
| Recombinant murine IL-4 | PeproTech | 214-14 |
| **Critical Commercial Assays** | | |
| CellTrace™ Far Red Proliferation Kit | ThermoFisher Scientific | C34564 |
| SuperSignal West | ThermoFisher Scientific | 34095, 34580 |
| **Experimental Models: Organisms/Strains** | | |
| Mouse: C57BL/6 | The Jackson Laboratory | JAX: 000664; RRID: IMSR_JAX:000664 |
| **Software and Algorithms** | | |
| FlowJo V10.8.1 | FlowJo LLC | N/A |
| FlowMax | Shokhirev et al., 2015 (Shokhirev and Hoffmann, 2013) | N/A |
| Python v3.7.164-bit base:conda | Anaconda v3.0 | N/A |

| REAGENT or RESOURCE | SOURCE | IDENTIFIER |
|---|---|---|
| ImageJ2 v2.9.0 | | N/A |
| Julia v1.9.3 | | N/A |
| R v4.2.0 | | N/A |

**Mice**

Mice were maintained in environmental control facilities at the University of California, Los Angeles. Female C57BL/6 mice in each replicate experiment were littermates, and were 8-13 weeks old unless otherwise indicated. Animal work was performed according to University of California, Los Angeles under approved protocols.

**B cell isolation and culture**

Spleens were harvested from 8–13-week-old female C57BL/6 mice. Homogenized splenocytes were incubated with anti-CD43 magnetic beads for 15 min at 4-8°C, washed with MACS buffer and passed through an LS column (Miltenyi Biotech). The purity of B cells was assessed at >97% based on B220 staining as described previously (Mitchell et al., 2018). Following isolation, B cells were stimulated with anti-CD40 (H: 10ug/mL, M: 3.3ug/mL, L: 1ug/mL), IL-4 (H: 20ng/mL, M: 6.6ng/mL, L: 2ng/mL), and anti-IgM (H: 10ug/mL, L: 1ug/mL), unless otherwise specified, and cultured for 4 days in fresh RPMI-based media at 37°C and 5% CO2. All anti-CD40 stimulation conditions mentioned in the results are stimulated with both anti-CD40 and IL-4 at corresponding doses.

**Immunoblot**

Cells were harvested from culture plates, washed in 1mL PBS and counted on a CytoFlex flow cytometer (CytoFLEX, Beckman Coulter), prior to preparing lysates for protein content analysis. Due to varying cell sizes and numbers over time as a result of growth and proliferation, an equal number of cells (as opposed to equal protein amounts) per sample was analyzed in each immunoblot. In cases where nuclear fractions were required to be separated, cells were first lysed in CE buffer on ice, followed by vortexing and centrifugation, and the supernatant containing the cytoplasmic fraction was removed. Nuclei were then lysed by 3 repeated freeze-thaw cycles between 37C water and dry ice, followed by centrifugation to clear the lysate of nuclear debris, after which the supernatant containing the nuclear fraction was harvested.

For immunoblotting, lysates were run on 4%–15% Criterion TGX pre-cast polyacrylamide gels (Bio-Rad), and transferred on to PVDF membranes using wet transfer. The following antibodies were used to identify the proteins of interest: RelA, cRel, Bcl-xL, p84 (loading control for nuclear lysates), and b-tubulin (loading control for cytoplasmic and whole cell lysates). Antibody details are given in the Resources table, and concentrations used were 1:5,000 for RelA and cRel, 1:1,000 for Bcl-xL, 1:10,000 for p84, and 1:10,000 for b-tubulin. Protein bands were detected using the Bio-Rad ChemiDoc XRS System, with a 10:1 mixture of the SuperSignal West Pico and Femto Maximum Sensitivity Substrates (Thermo Scientific) applied to detect chemiluminescence released by HRP-labeled secondary antibodies.

RelA, cRel, and Bcl-xL bands were quantified by measuring mean gray value using ImageJ2, deducting background value per lane (measured by a box of the same size directly below the target protein band), and normalizing intensities to the 0hr baseline.

**Media and buffer compositions**

B cell media: RPMI 1650 (Gibco) supplemented with 100 IU Penicillin, 100 µg/ml Streptomycin, 5 mM L-glutamine, 20 mM HEPES buffer, 1mM MEM non-essential amino acids, 1 mM Sodium pyruvate, 10% FBS, and 55 µM 2-Mercaptoethanol.
MACS buffer: Phosphate buffered saline, (pH 7.4) and 2% bovine serum albumin.
CE Buffer: 50 mM HEPES-KOH pH 7.6, 140 mM NaCl, 1 mM EDTA, 0.5% NP-40, freshly supplemented with EDTA-free protease inhibitors (5mM DTT, 1mM PMSF).
NE Buffer: 10 mM Tris-HCl, pH 8.0, 200 mM NaCl, 1 mM EDTA, freshly supplemented with EDTA-free protease inhibitors (5mM DTT, 1mM PMSF).

**Measurement of generation-specific B cells by CTFR staining**

B cells were stained with Cell Trace Far Red (CTFR) using CellTrace Far Red Cell Proliferation Kit (ThermoFisher Scientific, # C34564) as described by the manufacturer protocol. Briefly, 2M cells were resuspended in 1mL RT PBS and incubated with 1µL CTFR for 25 min at RT with rotation. Cells were washed by centrifugation, resuspension in 1mL RPMI with 10% FBS, and incubation for 10 min at RT. The washing steps were repeated 2 more times. CTFR labeled cells were treated with anti-CD40, IL-4, and / or anti-IgM for 96hrs as described above. The cells were harvested at indicated time points and acquired on the CytoFlex flow cytometer (CytoFLEX, Beckman Coulter). The cells were gated based on forward scatter (FSC) and side scatter (SSC) to identify live single cells. Doublets were then excluded from the analysis using FSC area and height. To deconvolve the cells into different generations based on dilution of CTFR, we used the Proliferation Modeling feature on FlowJo V10.8.1. Specifically, generation-0 cells were gated as "Undivided" in the APC-A channel according to the unstimulated control and 24hr samples, and the number of peaks were set based on visual estimation and then further adjusted based on the Peak Ratio and Root Mean Squared outputs to optimize curve fitting.

**Computational modeling of the T-dependent receptor signaling pathway**

The mathematical model of T-dependent (TD) B cell stimulation was developed in two parts. First, we expanded the previously published BCR-signaling ODE model (Shinohara *et al.*, 2014; Inoue *et al.*, 2016) by including the BCR receptor antigen binding (Fig. 1A left side), and scaled the parameters to match the units ($nM^{-1}$ $hr^{-1}$) in the rest of our model. The Shinohara and Inoue models prescribed a signal function for the CBM complex, a downstream adaptor for BCR receptor. We bridged the gap between antigen concentration and CBM signaling with a few additional ODE equations, and tuned these additional parameters (Table 1) such that the signaling dynamics matched the previous version:

$$\frac{d}{dt}[ANTIGEN] = -\varphi_1 * [ANTIGEN] - \varphi_4[ANTIGEN] * [BCR] * C_{c2m} + \varphi_5 * [ABCR] * C_{c2m}$$

$$\frac{d}{dt}[BCR] = \varphi_2 - \varphi_3 * [BCR] - \varphi_4 * [ANTIGEN] * [BCR] + \varphi_5 * [ABCR]$$

$$\frac{d}{dt}[ABCR] = \varphi_4[ANTIGEN] * [BCR] - \varphi_5 * [ABCR] - \varphi_6 * [ABCR]$$

where $[ANTIGEN]$, $[BCR]$, and $[ABCR]$ are the concentrations of the antigen, BCR, and their complex; $\varphi_i$, $i = 1,2,3, \ldots$, are the reaction constants (index are listed in Table 1); $C_{c2m} = 0.01$ is a scaling factor for external ligands like ANTIGEN to convert cellular concentration to media concentration. In this model, $[ANTIGEN]$ is the model input corresponds to experimental stimulation $\alpha$-BCR. As output of the BCR receptor module, $[ABCR]$ regulates CBM complex activation (Fig. 1A left side).

Next, we abstracted the CD40 model from its known signaling pathway (Elgueta *et al.*, 2009; Akiyama, Shinzawa and Akiyama, 2012) in a parsimonious way. As mentioned in the discussion, to avoid the complexity of combinatorial biochemical reactions among the TRAF complexes, we used TRAF3 to represent the TRAF2-TRAF3 complex that constitutively inhibits

the noncanonical NFκB pathway, and TRAF6 to represent the TRAF1-TRAF2, TRAF3-TRAF5, and TRAF6-TRAF2 complexes that all activate the canonical NFκB pathway.

$$\frac{d}{dt}[CD40L] = -\varphi_{11} * [CD40L] - \varphi_{14}[CD40L] * [CD40R] * C_{c2m} + \varphi_{15} * [CD40LR] * C_{c2m}$$

$$\frac{d}{dt}[CD40R] = \varphi_{12} - \varphi_{13} * [CD40R] - \varphi_{14} * [CD40L] * [CD40R] + \varphi_{15} * [CD40LR]$$

$$\frac{d}{dt}[CD40LR] = \varphi_{14}[CD40L] * [CD40R] - \varphi_{15} * [CD40LR] - \varphi_{16} * [CD40LR]$$

$$\frac{d}{dt}\left[TRAF6_{off}\right] = -\varphi_{17} * [CD40LR] * \left[TRAF6_{off}\right] + \varphi_{18} * [TRAF6_{on}]$$

$$\frac{d}{dt}[TRAF6_{on}] = \varphi_{17} * [CD40LR] * \left[TRAF6_{off}\right] - \varphi_{18} * [TRAF6_{on}]$$

$$\frac{d}{dt}[TRAF3] = \varphi_{19} * [TRAF3] - \varphi_{20} * [TRAF3] - \varphi_{21} * [CD40LR] * [TRAF3]$$

The subsequent kinases that further relay the receptor signal to NFκB signaling are TAK1 (for TRAF6) and NIK (for TRAF3). We used a Hill function for TRAF3-induced degradation of NIK to abstract a more complicated complex formation process:

$$\frac{d}{dt}[NIK] = \varphi_{35} - \varphi_{36} * [NIK] - \varphi_{37} * [NIK] * \frac{[TRAF3]^2}{[TRAF3]^2 + 0.5^2}$$

To generate heterogeneous cell responses, the receptor parameter values were distributed in each virtual B-cell the same way as the NFkB signaling module in previous publication, where synthesis, degradation, association, dissociation rates were drawn from a normal distribution with mean values from the standard parameter set (Table 1) and CV of 11.2% (Mitchell *et al.*, 2018). These ODEs (with 37 parameters and 12 species) were solved using the Tsit5 solver algorithm from the DiffEq.jl package in Julia, with an absolute error tolerance of 1e-5 and relative error tolerance of 1e-3. All simulations were carried out on an Ubuntu server with 64 threads, 2.1 to 3.7 GHz speed, and 384 GB RAM.

**Multiscale modeling coupling signaling network and B cell proliferation**

The receptor-extended TD model constructed above was combined with a published MATLAB model of B cell proliferation to create a multiscale model capable of simulating the division and death of a population of individual B-cells upon TD stimulation. The B cell model integrates a biophysically accurate model of canonical NFκB signaling (with about 300 parameters and 61 species) with models of the cell cycle (with 52 parameters and 23 species) and apoptosis (with 117 parameters and 59 species) (Shokhirev *et al.*, 2015; Mitchell *et al.*, 2018) to create a multiscale model capable of simulating the division and death of a population of individual cells upon T-dependent stimulation. Cleaved PARP (cParp) in the apoptosis model and cadherin-1 (Cdh1) concentration thresholds in the cell cycle model triggered virtual B-cell death and division, respectively. We translated the model from MATLAB into Julia 1.9.3 for faster execution. All reactions and parameters within the NFκB, apoptosis and cell cycle networks were maintained and distributed as described by Mitchell et al. (Mitchell *et al.*, 2018), except for 2 parameters in the cell cycle network that were changed to reduce the discrepancy between CD40 and CpG-induced proliferative response (Fig. S2, see more details in “Local sensitivity analysis to tune CD40-activated cell fates” section of the Methods).

Separate modules of the multi-scale model were employed when simulating for different purposes. For the NFκB dynamics in figure 1, only the receptor-NFκB model was used for the simulation, and the cell fate modules (apoptosis and cell cycle) were excluded. For Fig. S2C-F when we tuned the CD40-activated cell fates, the cell death module was excluded to enable faster turnaround for parameter tuning in the cell cycle module. For Fig. 5B-D, the cell cycle

module was excluded to isolate the effects of BCR signaling on cell survival. All the other model simulation used the full multi-scale model. When we reported the population trajectory of NFκB activity in Fig. 1E-H, all 1000 cells contributed to the mean and standard deviation, but in Fig. 4G-J, only cells that are alive at each timepoint contributed to the mean and standard deviation.

All of the code to run the model simulations and plot the figures is provided on GitHub (https://github.com/helengracehuang/BCR-CD40-integration). For each virtual B-cell with its own set of parameters, we ran the model in two phases to first identify the steady state, and then simulate the dynamic time course upon stimulation, with initial states from this steady state. The steady state was solved using Julia's steady state Tsit5 solver with an absolute error tolerance of 1e-5 and relative error tolerance of 1e-3. The simulation time for which the given ODE reach steady state was limited within 800hrs.

**Computational modeling of the BCR-induced cell death pathway**

Since we found α-BCR stimulation had an NFκB-independent anti-survival effect that overrides its NFκB-dependent pro-survival effect (Fig. 3), we decided to resolve this difference by modifying the multi-scale model. It was reported that ligation of the BCR induces cell death in some B cells (Graves, Craxton and Clark, 2004) due to activation of Bcl-2 Interacting Mediator of cell death (Bim) (Gao, Kazama and Yonehara, 2012), caspase-2 or -8 (Chen *et al.*, 1999), mitochondrial dysfunction (Akkaya *et al.*, 2018) or more. Based on these signaling mechanisms that may mediate activation-induced cell death (AICD) in B-cells and the available species in the existing cell death module, we revised the cell death module of the T-dependent multi-scale B-cell model to include a simplified pathway from activated BCR to caspase-8 processing (Fig. 4A):

$$\frac{d}{dt}[PC8] = \left(original\ \frac{d}{dt}[PC8]\right) - \varphi_{C8,AICD} * [PC8] * [ABCR]$$

$$\frac{d}{dt}[C8] = \left(original\ \frac{d}{dt}[C8]\right) + \varphi_{C8,AICD} * [PC8] * [ABCR]$$

where $[PC8]$, $[C8]$, and $[ABCR]$ are the concentrations of the pre-caspase-8, caspase-8, and activated BCR; $original\ \frac{d}{dt}[PC8]$ and $original\ \frac{d}{dt}[C8]$ are the original differential equations for pre-caspase-8 and caspase-8 in Mitchell *et al.*, 2018, abbreviated to highlight the revision we made; $\varphi_{C8,AICD}$ was tuned to be 0.00021 according to experimental data of BCR-CD40 costimulation versus CD40-only stimulation conditions (Fig. 4B-C).

Simulations prior to figure 4 and Fig. 5F-H did not include this BCR-induced cell death pathway. Fig. 4B-F, Fig. 5A-E, I-K, and figures 6 and 7 were all simulated with the modified caspase-8 equations.

**Model fit evaluation**

Root-mean-squared deviation (RMSD) were calculated on the population dynamics between model simulation and experimental results (Fig. 2F, S2B, 3E, 3F, and 4D) and between two experimental conditions (Fig. 3H,K) in the same manner. Two RMSD scores, one for population expansion index (Fig. 2D), and the other for generational composition (Fig. 2E) between each pair of model and experimental outputs at each experimental timepoint (0, 24, 36, 48, 72, and 96hrs) were calculated.

For the RMSD on generational composition:

$$RMSD_{gen} = \sqrt{\sum_{i=1}^{5}\sum_{j=0}^{6}\left(\frac{n_{i,j}}{N_i} - \frac{\hat{n}_{i,j}}{\hat{N}_i}\right)^2}$$

Where $i$ is the $i$-th timepoint of the experimental measurement (i.e. $i = 1$ corresponds to the measurement at 24 hours, followed by 36, 48, 72, and 96 hours), and $j$ is the generation number, ranging from generation 0 to 6 corresponding to founder cells to cells that have divided 6 times. $n_{i,j}$ thus means the number of live cells in generation $j$ and timepoint $i$ in the experimental data, while $\hat{n}_{i,j}$ is the corresponding live cell number in generation $j$ and timepoint $i$ in model simulation. Additionally, $N_i = \sum_{j=0}^{6} n_{i,j}$ represents the total number of live cells at timepoint $i$ in the experimental data, and $\hat{N}_i = \sum_{j=0}^{6} \hat{n}_{i,j}$ represents the corresponding total live cell number in model simulation. $\frac{n_{i,j}}{N_i}$ and $\frac{\hat{n}_{i,j}}{\hat{N}_i}$ are thus the generation decomposition ratios at each time point for experimental data and simulation data, respectively.

For population expansion, the RMSD is composed of two parts, one normalized to population size at 0 hour ($N_0$) and one normalized to the population size at 24 hours ($N_1$) to account for unpredictable mechanical cell death (which typically occur within the first few hours) as a form of technical error in experiments. Both RMSD scores are then normalized to the number of timepoints (5 timepoints for 0hr normalization, and 4 timepoints for 24hr normalization) and the maximum population expansion so that different amount of population expansion at different doses are evaluated on the same scale:

$$RMSD_{pop\_exp} = \sqrt{\frac{\sum_{i=1}^{5}\left(\frac{N_t}{N_0} - \frac{\hat{N}_t}{\hat{N}_0}\right)^2}{5 \cdot \max\limits_{i=1,\ldots,5} N_i}} + \sqrt{\frac{\sum_{i=2}^{5}\left(\frac{N_t}{N_1} - \frac{\hat{N}_t}{\hat{N}_1}\right)^2}{4 \cdot \max\limits_{i=2,\ldots,5} N_i}}$$

**Local sensitivity analysis to tune CD40-activated cell fates**

Due to the discrepancy between CD40 and CpG-induced proliferative response, we quantified several key variables in the dye dilution data that determined the population dynamics with FlowMax (Shokhirev and Hoffmann, 2013). After fitting FlowMax model to the experimental data, we quantified the time to first division (Tdiv0), time to later divisions (Tdiv1+), and the fraction of generation 0 cells that respond by dividing (F0) in response to low, medium, and high CD40 doses. In all CD40 doses, the average Tdiv0 is much later and more dose-specific (68.5 to 76.9hrs since stimulation onset for high to low dose of CD40) than what the model predicted (36.1 to 40.6hrs). On the other hand, the average Tdiv1+ of the CD40 experimental data were mostly shorter than predicted by the model (Table S1 Exp vs Model(1), Fig. S2A), and the proportion of dividers was lower, indicated by a larger amount of cells in generation 0 at 96hrs in Fig. S2A and a smaller F0 quantified by FlowMax than the model predicted (Table S2 Exp vs Model(1).

To improve model fit, we identified locally sensitive parameters in the cell cycle module that contribute to Tdiv0 and Tdiv1+ by calculating the standard deviation in division times when scaling each parameter by 0.2, 0.33, 0.4, 0.5, 0.66, 1.0, 1.5, 2.0, 2.5, 3.0, or 5.0-fold. 2 out of 55 parameters stood out as the best candidates for tuning Tdiv0 and Tdiv1+: retinoblastoma (Rb) decay rate and cyclin B (CycB) synthesis rate, respectively (Fig. S2C). Rb decay rate was tuned to be 10% of the original value, whereas CycB was tuned to be 1.8-fold the original value to achieve a later and more dose-responsive Tdiv0, shorter Tdiv1+, and smaller divider percentage (Fig. S2D,E,F).

A simulation of 300 cells with distributed parameters before and after parameter tuning showed that mean Tdiv0 for dividers increased from 36.14 hours to 62.80 hours for high dose of CD40 stimulation, and from 40.65 hours to 74.78 hours for low dose, achieving both a later and more dose-responsive Tdiv0, resulting in much more agreement with the FlowMax output based on experimental data (Table S1, left 3 columns). The mean Tdiv1+ for dividers decreases from around 9 hours to 6 hours for all doses, which is in concordant with high dose of CD40, but in less agreement with medium and low doses (Table S1, right 3 columns). Table S2 also showed the percentage of dividers out of all founder cells decreased for all doses, while maintaining CD40 dose-responsiveness.

**Table S1. Experimental vs. Model proliferation time before (1) & after (2) tuning**

| Condition | EXP Tdiv0 | MODEL(1) Tdiv0 | MODEL(2) Tdiv0 | EXP Tdiv1+ | MODEL(1) Tdiv1+ | MODEL(2) Tdiv1+ |
|---|---|---|---|---|---|---|
| **CD40 high** | 68.5 | 36.1 | 60.7 | 6.1 | 9.0 | 6.2 |
| **CD40 medium** | 68.6 | 35.7 | 66.2 | 7.8 | 9.2 | 6.0 |
| **CD40 low** | 76.9 | 40.6 | 79.4 | 35.2 | 9.7 | 6.3 |

**Table S2. Experimental vs. Model divider percentage before (1) & after (2) tuning**

| Condition | EXP F0 | MODEL(1) F0 | MODEL(2) F0 |
|---|---|---|---|
| **CD40 high** | 46.8% | 58.3% | 46.3% |
| **CD40 medium** | 18.4% | 46.3% | 34.7% |
| **CD40 low** | 4.4% | 24.0% | 21.0% |